

# High-thermally conductive AlN-based microwave attenuating composite ceramics with spherical graphite as attenuating agent

Xia Fang (✉ [fushanfangxia@sina.com](mailto:fushanfangxia@sina.com))

Nanjing Tech University

Lei Jiang

Nanjing Tech University

Limei Pan

Nanjing Tech University

Shuang Yin

Nanjing Tech University

Tai Qiu

Nanjing Tech University

Jian Yang

Nanjing Tech University

---

## Research Article

**Keywords:** Spherical graphite, Aluminum nitride, Thermal conductivity, Dielectric property, Microwave absorption

**Posted Date:** December 4th, 2020

**DOI:** <https://doi.org/10.21203/rs.3.rs-63995/v3>

**License:** © ⓘ This work is licensed under a Creative Commons Attribution 4.0 International License.

[Read Full License](#)

---

**Version of Record:** A version of this preprint was published at Journal of Advanced Ceramics on March 1st, 2021. See the published version at <https://doi.org/10.1007/s40145-020-0441-2>.

# **High-thermally conductive AlN-based microwave attenuating composite ceramics with spherical graphite as attenuating agent**

Xia Fang<sup>a, b</sup>, Lei Jiang<sup>a, b</sup>, Limei Pan<sup>a, b</sup>, Shuang Yin<sup>a, b</sup>, Tai Qiu<sup>a, b</sup>, Jian Yang<sup>a, b, \*</sup>

a Jiangsu Collaborative Innovation Center for Advanced Inorganic Function Composites, China;

b College of Materials Science and Engineering, Nanjing Tech University, Nanjing 211816, China

\*Corresponding author: E-mail: [yangjian1976@163.com](mailto:yangjian1976@163.com) (Jian Yang)

**Abstract:** High-thermally conductive AlN-based microwave attenuating composite ceramics with spherical graphite (SG) as the attenuating agent were fabricated through hot-pressing sintering. The SG maintains its three-dimensional morphology within the sintered bodies, which considerably impedes the sintering of the composites to some extent but slightly influences on the growth of AlN grains. The addition of SG reduces the strength of the composites, but provides a moderate toughening effect at the optimal addition amount (3.8 MPa·m<sup>1/2</sup> at 4 wt% SG). Benefiting from the low anisotropy, high thermal conductivity, and the three-dimensional morphology of SG, the composites exhibit a relatively higher thermal conductivity (76.82 W·m<sup>-1</sup>·k<sup>-1</sup> at 10 wt% SG) compared with composites added with non-spherical attenuating agent. The dielectric constant and loss (8.2–12.4 GHz) increase remarkably as the amount of SG added increases up to 8 wt%, revealing that the incorporation of SG improves the dielectric property of the composite. The composite with 7 wt% SG exhibits the best absorption performance with a minimum reflection loss of -14 dB at 12.4 GHz and an effective

absorbing bandwidth of 0.87 GHz. The excellent overall properties of the SG/AlN microwave attenuating composites render them as a promising material for various applications. Moreover, SG has a great potential as an attenuating agent for microwave attenuating composites due to its strong attenuation upon integration, high thermal conductivity, and low anisotropy.

**Keywords:** Spherical graphite; Aluminum nitride; Thermal conductivity; Dielectric property; Microwave absorption

## **1 Introduction**

A microwave attenuating material is a vacuum electronic material which is crucial in radars, early-warning aircrafts, and microwave measurement systems [1–6]. It absorbs electromagnetic waves within specific frequency bands and converts them into heat energy for the inhibition of sideband oscillation, broadening of bandwidth, and improving electromagnetic matching during operations. With the fast development of vacuum electronic devices into extreme application conditions such as high frequency, high power, and high temperature, it is indispensable for microwave attenuating materials to have a high thermal conductivity, in addition to an excellent microwave absorption capability, to enable them to conduct the heat energy efficiently and avoid damage to working devices caused by high temperature.

As a result of their outstanding characteristics such as high thermal conductivity, good mechanical properties, high-temperature stability, and moderate dielectric constants, ceramic-based composite attenuating materials, such as BeO, MgO, Al<sub>2</sub>O<sub>3</sub>, and AlN matrix composite ceramics, have been one of the extensively for attenuation

materials [1]. Wherein AlN has been regarded as the most advantageous attenuating ceramic matrix by virtue of its high thermal conductivity ( $320 \text{ W}\cdot\text{m}^{-1}\cdot\text{K}^{-1}$ ), high strength, high insulation, non-toxicity, and low out-gassing under a vacuum environment [1,2]. The preparation of AlN-based microwave attenuating composite ceramics generally involves the introduction of metal conductors (W and Mo), semiconductors (SiC and  $\text{TiO}_2$ ), or carbonaceous materials (graphite, carbon black, graphene and carbon nanotubes) to improve the dielectric loss of the AlN-based composites, and enhance their microwave attenuation [3,4]. However, the thermal conductivity of AlN ceramics is highly sensitive to the introduction of a second phase, and all the pores, interfaces, grain boundary impurities, and crystal defects resulting from the addition of the attenuating agent greatly reduces the thermal conductivity of AlN-based composites [7–9].

To improve the thermal conductivity of AlN-based attenuating composites, highly thermally conductive metal attenuating agents have been employed. However, the inhomogeneous microstructure induced by the mismatching density between the AlN matrix and the metallic materials inevitably affects the thermal stability of the composite material. The wide band gap semiconductor SiC has been widely applied as an attenuating agent for preparing AlN-based attenuating composite ceramics. However, the addition of SiC not only increases the heterogeneous interface, but also generates a SiC/AlN solid solution. As a result, the SiC/AlN composites develop a large interface, high thermal resistance, and numerous crystal defects, which would cause severe phonon scattering and the deterioration of thermal conductivity of the SiC/AlN

composite attenuating ceramics [1,10,11].

In recent years, the lightweight carbonaceous nanomaterials with high electrical and thermal conductivity such as graphene and carbon nanotubes (CNTs), have been considered as promising attenuating agents for the preparation of ceramics matrix microwave attenuating composite materials [12–19]. Several studies have found that a small amount of incorporated graphene and CNTs greatly improves electrical conductivity and dielectric properties of AlN-based composite materials [7–9], making them potentially suitable attenuating agents for the preparation of AlN-based composite materials. Liang et al. [20] reported that, within the frequency range of 26.5–40.0 GHz, both the dielectric constant and dielectric loss of AlN/CNT composites increased significantly as the CNT content increased, and a high dielectric loss of 0.1–0.61 was achieved at 5 vol% CNT. Nonetheless, as CNTs have a very large specific surface area and a hollow tubular structure, they can adsorb a large amount of gas and may undergo out-gassing under a high vacuum environment, thus limiting their application in preparing vacuum electronic materials [21,22]. Graphene has an ultra-high thermal conductivity along the in-plane direction, while its layered structure readily produces a large heterogeneous interface between AlN matrix and graphene, which greatly reduces the thermal conductivity of AlN/graphene composite materials [7, 8]. Yin et al [23] reported that the thermal conductivity of graphene platelets/AlN composites sharply decreased from 58.21 to 13.84  $\text{W}\cdot\text{m}^{-1}\cdot\text{K}^{-1}$  as the graphene content increased from 0 to 9.5 wt%. In addition, one/two-dimensional (1/2D) carbonaceous nanomaterials are generally anisotropic [7,24], which is detrimental to the uniform heat dissipation of the

material. Although various potential attenuating agents, such as metal conductors, semiconductors, and carbonaceous materials, have been studied, none of them are suitable for the preparation of a highly thermally conductive AlN-based attenuating composite materials with no anisotropy. To improve the work reliability of microwave attenuating materials in future work, it is important to exploit an attenuating agent that can satisfy the demand of combined high thermal conductivity, strong attenuation and low anisotropy.

Among the previously reported attenuating agents, graphite is a traditional carbonaceous material with an excellent electrical conductivity ( $\sim 10^6$  S/m), thermal conductivity ( $\sim 2200$  W·m<sup>-1</sup>·K<sup>-1</sup>) [25], high thermal stability and low cost, hence, it is considered as a promising material for the preparation of materials with strong attenuation [26–34]. Historical studies have shown that the introduction of a small amount of graphite can improve the dielectric and microwave absorption properties of the composites incorporated with graphite [29–34]. Torgut et al. [32] found that the incorporation of graphite into a polymer matrix significantly enhanced the polarization loss of the composites, and the  $\epsilon'$  value of the 10 wt% composite was 80.5 higher than that of the monolithic polymer material. Sun et al. [33] fabricated SiC/graphite composites based on a porous SiC matrix, and they found that introducing graphite from 1 wt% to 7 wt% increased the electrical conductivity of the composite by five orders of magnitude. Moreover, the incorporation of graphite resulted in the multiple reflection of the electromagnetic waves inside the material, improving the electromagnetic shielding performance of the SiC/graphite composite. Zhang et al. [34] observed that when the

graphite/geopolymer ratio was 12, the minimum reflection loss ( $RL_{\min}$ ) of the graphite/geopolymer composite reached -65 dB at a frequency range of 2–18 GHz and at a thickness of 4.15 mm. However, the application of graphite in preparing AlN-based microwave attenuating composite material has not been reported in detail until now. Moreover, in all of the reports on composite absorption materials filled with graphite, the flake graphite is the dominantly employed. Coinciding with its 2D structure of two-dimensional materials, the high aspect ratio of flake graphite can also result in numerous heterogeneous interfaces inside the matrix, just like graphene, thereby limiting the improvement of the thermal conductivity of the composite. Moreover, the composites filled with 2D flake graphite also suffer from the anisotropic thermal, electricity, and dielectric properties [25, 35–38]. For example, Li et al. [38] employed the squeeze casting method to fabricate graphite flakes/Al composites and found that as the graphite content varied from 40 to 70 vol%, the thermal conductivity of the composites increased from 544 to 714  $W \cdot m^{-1} \cdot K^{-1}$  in the direction parallel to the plane of the graphite layers but decreased from 104 to 31  $W \cdot m^{-1} \cdot K^{-1}$  in the direction perpendicular to the plane of the graphite layers, resulting from the high interfacial thermal resistance, low thermal conductivity (6  $W \cdot m^{-1} \cdot K^{-1}$ ) and the anisotropy caused by the addition of flake graphite. This suggests that there is a great limitation on the preparation of high-performance microwave attenuating materials with high thermal conductivity and low anisotropy when flake graphite is employed as the attenuating agent. And to the best of our knowledge, which remains a great challenge to date.

In this work, considering the high electrical and thermal conductivities and the

microwave absorption property of graphite, spherical graphite, instead of the traditional flake graphite, was chosen as the attenuating agent in the preparation of AlN-based composite ceramics with strong attenuation, high thermal conductivity, and low anisotropy. SG is a granulated form of graphite, which not only enjoys excellent thermal and electrical properties similar to flake graphite, but also has a low anisotropy as opposed to flake graphite. More importantly, the spherical morphology of SG results in its relatively small aspect ratio, which can potentially reduce the heterogeneous interfaces between the graphite particles and the AlN matrix and their adverse effect of interfacial thermal resistance on the thermal conductivity of the composites. Owing to its high electrical conductivity, low specific surface area, chemical resistance, high crystallinity and high theoretical lithium insertion capacity, SG is widely utilized to as a substitute for the traditional flake graphite for the preparation of the battery negative electrodes [39,40]. Regrettably, as far as we know, there are few reports on the preparation of ceramic matrix composites filled with spherical graphite.

To explore the potential and feasibility of employing SG as highly effective attenuating agent for the preparation of AlN-based microwave attenuating composite materials, the effects of the mass fraction of SG on the sintering, mechanical, thermal, dielectric, and absorption properties of the SG/AlN composites were systematically studied. The obtained SG/AlN composites exhibited a low anisotropy, excellent thermal conductivity, and strong dielectric loss and absorption ability, which demonstrate their potential as high-performance attenuation materials for future application after further optimization.

## 2 Experimental Process

### 2.1 Preparation of SG/AlN composite ceramics

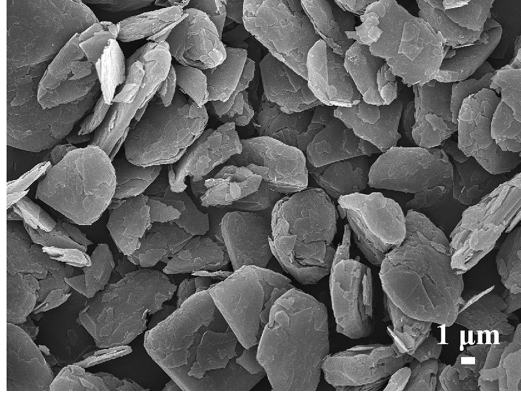


**Fig. 1 Micro-morphology of spherical graphite raw material**

Commercial AlN (1–2  $\mu\text{m}$ , Liaoning Desheng Special Ceramics Manufacturing Co., Ltd), Y<sub>2</sub>O<sub>3</sub> ( $d_{50}$  = 7  $\mu\text{m}$ , purity 99.95 %, Shanghai Yuelong Chemical Factory), and SG ( $d_{50}$  = 6  $\mu\text{m}$ , Qingdao Haida Graphite Co., Ltd.) were used as the raw materials. The microscopic morphology of the spherical graphite is depicted in Figure 1. The SG particles are oval, and they have a significant difference from the layer structure of flake graphite.

The amount of the sintering aid Y<sub>2</sub>O<sub>3</sub> was fixed at 4 wt%, and the SG content was varied from 0 to 16 wt%. The preparation process of the SG/AlN composites is schematically shown in Figure 2. First, the AlN and Y<sub>2</sub>O<sub>3</sub> powders was ball-milled for 4 h in a planetary ball mill at a rotating speed of 160 rpm. Thereafter, they were dried at 80 °C for 24 h, ground, and then sieved through a size 60 mesh. Varying amounts of SG powder was mixed with the AlN-Y<sub>2</sub>O<sub>3</sub> composite powder in anhydrous ethanol, and the mixture was combined under magnetic stirring (S10-3, Shanghai Sile Equipment Co., Ltd., China) and mechanical stirring (JJ-1, Jiangyin Poly Research Equipment Co., Ltd., China) for 2.5 h at 750 rpm. The mixture was dried at 120 °C for 8 h, and the resultant

powders were sieved through a size 60 mesh. The as-prepared composite powders with different SG contents were loaded into graphite molds and then hot-pressing sintered under a nitrogen ( $N_2$ ) atmosphere, with a sintering temperature of 1900 °C, uniaxial pressure of 25 MPa, and holding time of 1 h. Finally, the as-sintered samples were cooled to room temperature and then taken out of their molds.

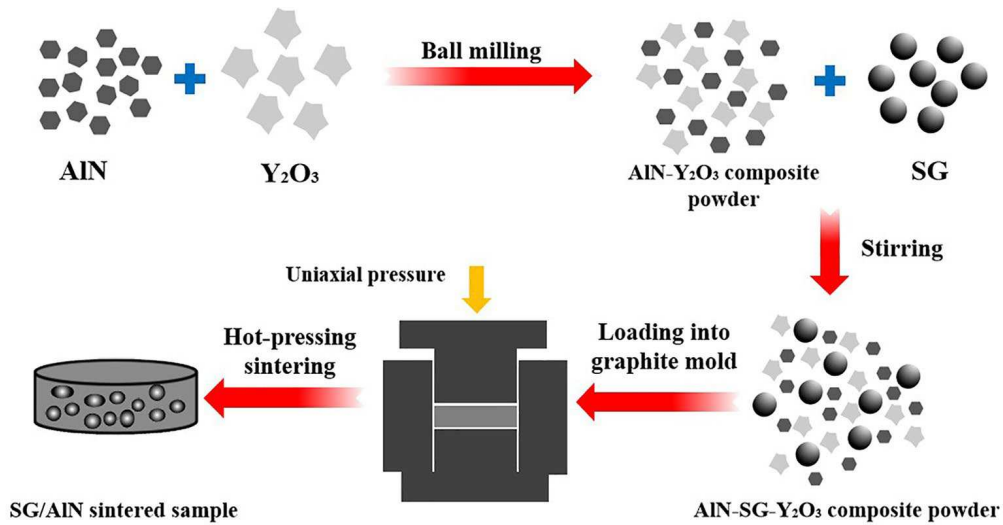


**Fig. 2 Schematic of the preparation process for fabricating the SG/AlN composites**

## 2.2 Testing and Characterization

The phase composition of the as-prepared SG/AlN composites was detected using X-ray diffraction (XRD, Smartlab, Japan) analysis. The X-ray photoelectron spectroscopy (XPS, AXIS Ultra DLD, Kratos, UK) was carried out to determine the chemical composition of the surface of the sample. The bulk density ( $\rho_b$ ) of the sintered sample was measured by Archimedes method, and then the bulk density of the sample was divided by the corresponding theoretical density ( $\rho_t$ ) to obtain the relative density ( $\rho_r$ ), i.e.,  $\rho_r = \rho_b / \rho_t$ , wherein the theoretical density of a fully dense composite was calculated in accordance with the rule of mixtures, assuming the densities of  $3.26 \text{ g}\cdot\text{cm}^{-3}$

for AlN,  $5.01 \text{ g}\cdot\text{cm}^{-3}$  for  $\text{Y}_2\text{O}_3$ , and  $2.25 \text{ g}\cdot\text{cm}^{-3}$  for SG. The flexural strength of the sample with a dimension of  $4 \times 3 \times 36 \text{ mm}^3$  was tested using the three-point bending method at a loading rate of  $0.5 \text{ mm}\cdot\text{min}^{-1}$ . To test the fracture toughness of the sample, the single edge notch beam method was carried out at a loading rate of  $0.05 \text{ mm}\cdot\text{min}^{-1}$  for a sample with dimensions of  $4 \times 2 \times 30 \text{ mm}^3$ , with a groove depth of 2 mm and width of 0.1 mm. A field emission scanning electron microscope (FESEM, SU8010, Hitachi, Japan) equipped with an energy dispersive system (EDS) was used to analyze the fracture morphology and chemical composition of the sample. The thermal diffusivity  $\alpha$  of the sample ( $\Phi 12.7 \text{ mm} \times 2 \text{ mm}$ ) was determined using a laser thermal conductivity meter (LFA447, Netzsch, Germany) under the protection of helium atmosphere, and the thermal conductivity  $\lambda$  of the sample was calculated by Equation (1) [41]:

$$\lambda = \alpha \times C_p \times \rho \quad (1)$$

where  $\rho$  is the bulk density of the sample, and  $C_p$  is the heat capacity. Each sample subjected to thermal analysis was tested for three times, and the mean value was calculated. To investigate the dielectric properties and microwave absorption properties of the samples, the waveguide method with a vector network analyzer was used to test the electromagnetic parameters of the sample ( $22.86 \times 10.16 \times 2.5 \text{ mm}^3$ ) in the X-band (8.2–12.4 GHz). The alternating-current (AC) impedance (1– $10^6$  Hz) of the sample was tested by electrochemical stations (CHI760E, China).

### 3 Results and Discussion

#### 3.1 Phase Composition

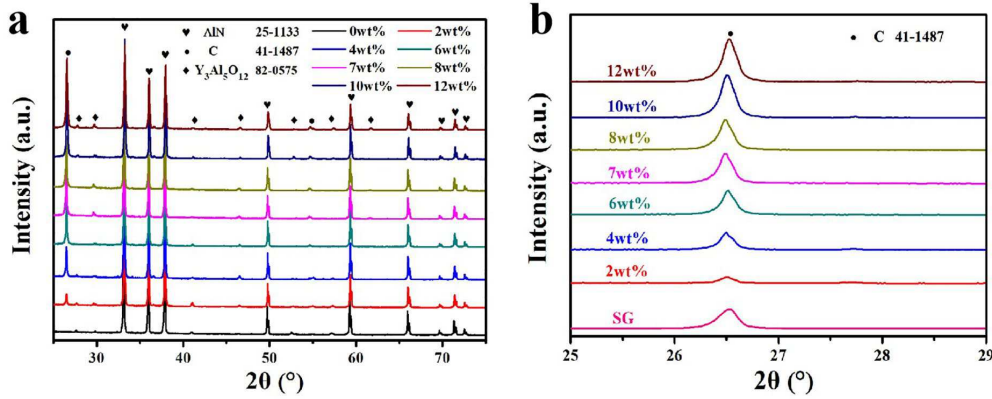


**Fig. 3 (a) XRD patterns of SG/AlN composites with different SG contents, (b) XRD patterns of SG raw powder and SG/AlN composites with different SG contents at 25 to 29 degrees**

The XRD patterns of the as-sintered SG/AlN composites with various SG contents are presented in Figure 3(a). The main phases in the monolithic AlN ceramic are AlN and  $Al_5Y_3O_{12}$ , while the main phases in the SG/AlN composites are AlN, carbon (C), and  $Al_5Y_3O_{12}$ . No other carbon-containing compound was detected, illustrating that SG did not react with any other phases during the sintering process. The XRD patterns of the SG raw material and SG/AlN composites with various SG contents within a small  $2\theta$  angle range are shown in Figure 3(b). Visibly, the diffraction peak of C becomes stronger as the SG content increases, and the position of the C diffraction peak in the composite material did not show a significant change with that in the SG raw material. This indicates that SG maintains as its original graphitic structure in the sintered sample. The existence of  $Y_3Al_5O_{12}$  is ascribed to be the reaction between  $Y_2O_3$  and  $Al_2O_3$  that exists on the surface of AlN, which not only promotes the liquid phase sintering of the AlN-based composite under a relatively low temperature, but also effectively removes the oxygen impurities in the lattice of AlN, thereby enhancing the thermal conductivity of the AlN-based composite ceramics [42,43].

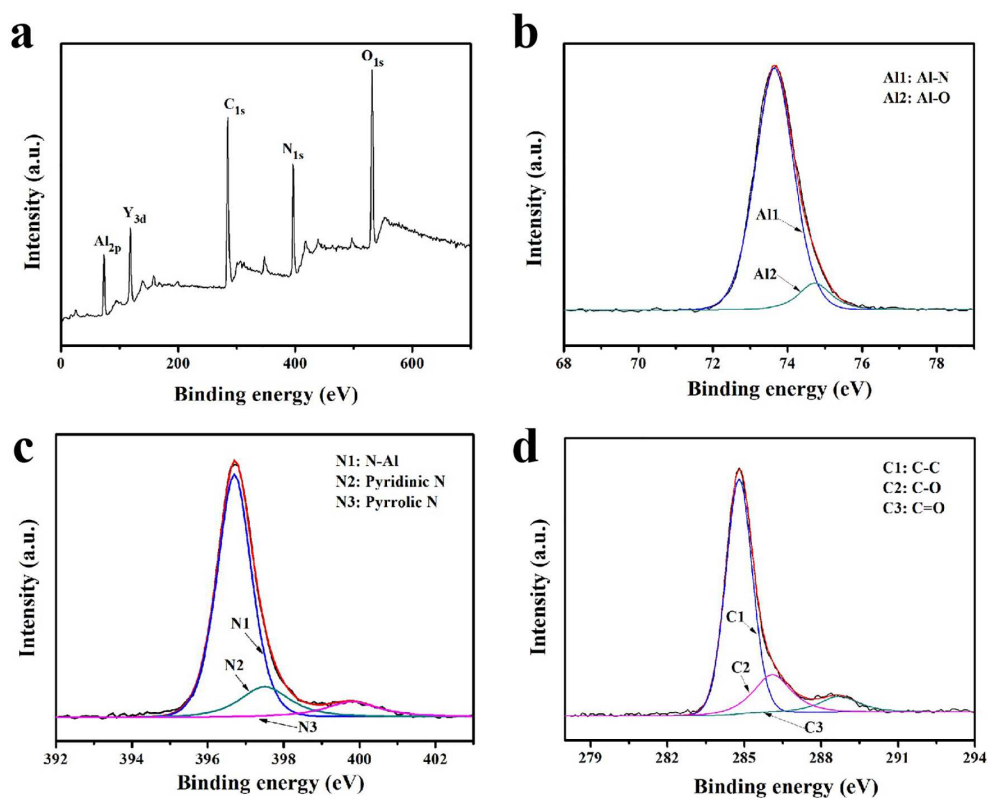


**Fig. 4 (a)** XPS survey spectra of 4 wt% composite, (b–d) are the spectra of Al 2p, N 1s and C 1s, respectively

To further identify the chemical forms and interactions of each element in the SG/AlN composite, the XPS survey spectra of the 4 wt% composite were obtained and presented in Figure 4. Several typical peaks for Al 2p, C 1s, N 1s, Y 3d, and O 1s can be clearly identified in Figure 4(a). In the XPS spectrum of Al 2p, as shown in Figure 4(b), the intensity of peaks at 73.65 eV and 74.73 eV correspond to the Al-N and Al-O bonds, respectively [44]. It can be inferred that the  $Y_3Al_5O_{12}$  is responsible for the formation of Al-O. The N element mainly exists in the form of the N-Al bond (396.7 eV) in the sintered body [44]. In addition, the two slight and minor peaks appear at 397.5 eV and 399.8 eV correspond to pyridinic N [45,46] and pyrrolic N [47], respectively. This may be attributed to that a few C atoms which were doped into the AlN lattice and replaced

the N atoms [48]. The C 1s spectrum can be divided into C-C (284.8 eV) [45,49], C-O (286.1 eV) and C=O (288.7 eV) bonds [50]. The presence of carbon-oxygen bonds may be due to a small amount of oxidation of graphite during the drying process. Nevertheless, no other C bonds were found in the composite, further confirming that SG still maintains its original graphitic structure within the sintered body, and no N doping of the SG occurred even after sintering under a N<sub>2</sub> protective atmosphere.

### 3.2 Sintering Properties and Microstructure

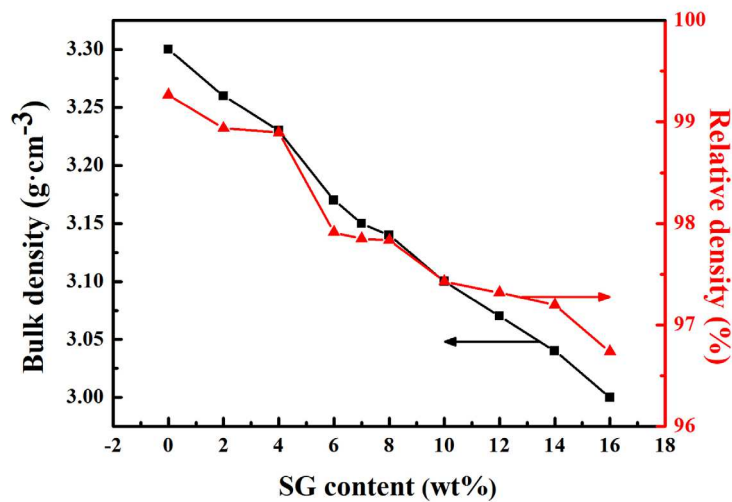


**Fig. 5 Bulk density and relative density of SG/AlN composites with different SG contents**

The bulk density and relative density of the SG/AlN composites with varying SG contents are shown in Figure 5. As the SG content increases from 0 wt% to 16 wt%, the bulk density and relative density of the composites decrease monotonously from 3.30 g·cm<sup>-3</sup> to 3.00 g·cm<sup>-3</sup> and 99.50 % to 96.73 %, respectively. The descend of relative density indicates that the SG addition significantly inhibits the sintering process of the SG/AlN composites. To explain the decrease in density of the composite as the amount of SG increases, the micro-morphology, location, and distribution of SG particles within the materials, the microstructure and chemical composition of the SG/AlN composites

were further characterized through SEM, EDS, and element mapping [48,51,52].

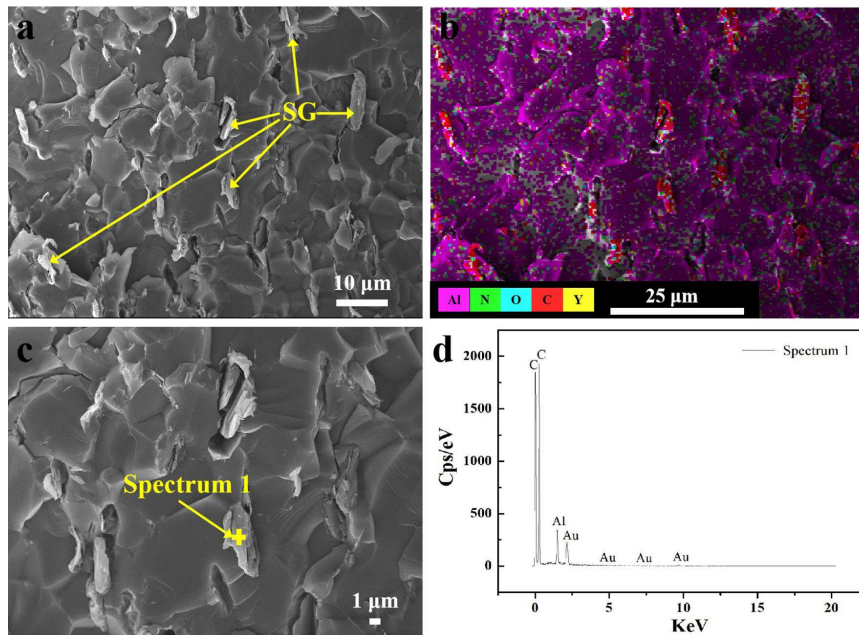


**Fig. 6 (a) Microstructure, (b) EDS mapping, (c) high-resolution microstructure and (d) EDS diagrams of 4 wt% SG/AlN composite without ultrasonic cleaning**

The SEM, EDS, and element mapping diagrams of the composite with 4 wt% SG are provided in Figure 6. The red area in Figure 6(b) indicates the SG particles, as confirmed by the combined analysis of element mapping and EDS. The SG particles, with a significantly different morphology from the AlN matrix, can be well distinguished in Figures 6(a) and (c). To more clearly observe the location and distribution of SG inside the AlN matrix, the fracture surfaces of the sintered samples with 0 wt% to 12 wt%SG, were ultrasonically cleaned and then characterized using SEM and EDS analysis. As is shown in Figure 7, the SG showed a clear fault-like structure after ultrasonication. Meanwhile, the fine AlN particles and SG particles on the fracture surface of the ultrasonicated sample were cleared away, showing a clearer fracture morphology in comparison with the non-ultrasonicated sample. Figure 8 shows

the fracture morphology of the composites containing different SG contents. Overall, the SG particles and AlN grains, although tightly bonded, showed significantly different morphologies, which can be clearly distinguished in all the composites. The SG particles were distributed homogeneously in the AlN matrix. Compared with that of the pristine SG shown in Figure 1, the micro-morphology of the SG inside the sintered sample suffered some damage and exhibited a pronounced deformation, which can be attributed to the uniaxial pressure applied during the sintering process. Nevertheless, most of the SG particles inside the composites maintain their three-dimensional morphology after sintering, which is an obvious distinction from the 2D morphology of flake graphite [25, 27, 33]. Besides, none of these composites exhibited a pronounced behavior based on orientation, whether parallel or perpendicular to the pressure directions inside the sintered body. This is obviously differed from the orientated flake graphite in the AlN/graphite composite reported by Zhang et al [25], suggesting that orientation alignment and anisotropy can be alleviated to some extent by using spherical graphite. Whereas, a significant agglomeration of SG particles can be observed in the composites with 10 wt% and 12 wt% SG, implying that at high SG contents, the SG particles experience an increased difficulty in dispersion.

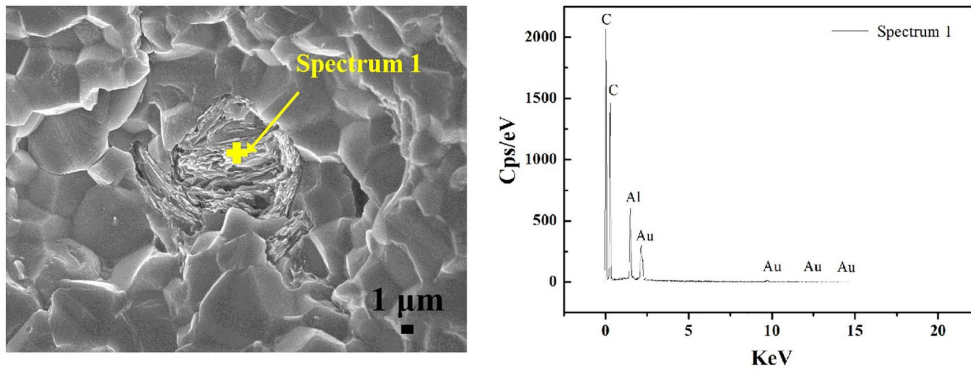


**Fig. 7 Microstructure (ultrasonic cleaning) and EDS diagrams of 4 wt% SG/AlN composite**

As shown in Figure 8, the average AlN grain size of a monolithic AlN ceramic is  $\sim 7$   $\mu\text{m}$ , while that of the composite with 12 wt% SG is 5  $\mu\text{m}$ . Compared to the decrease in the AlN grain size from 6.5  $\mu\text{m}$  to 3.5  $\mu\text{m}$ , as the graphene content increased from 0 to 7.28 vol% (5 wt%), in graphene/AlN composites prepared via hot-pressing sintering [8], the introduction of SG into the AlN matrix only slightly inhibited the growth of AlN grains, which may be ascribed to the lower SG/AlN grain boundary interface in SG/AlN composites relative to that of the AlN-based composites containing 2D flake materials. The fewer SG/AlN interfaces sufficiently decrease the adverse impact of the incorporation of SG on the AlN mass transfer, thereby alleviating the inhibition of AlN grain growth. As the amount of SG incorporation increases, the SG/AlN heterogeneous interface grows and has a non-negligible effect on the mass transfer process of AlN and the migration process in the AlN grain boundary. These hinder the sintering process of the materials, increasing the number of pores within the material and accordingly decreasing the densification.

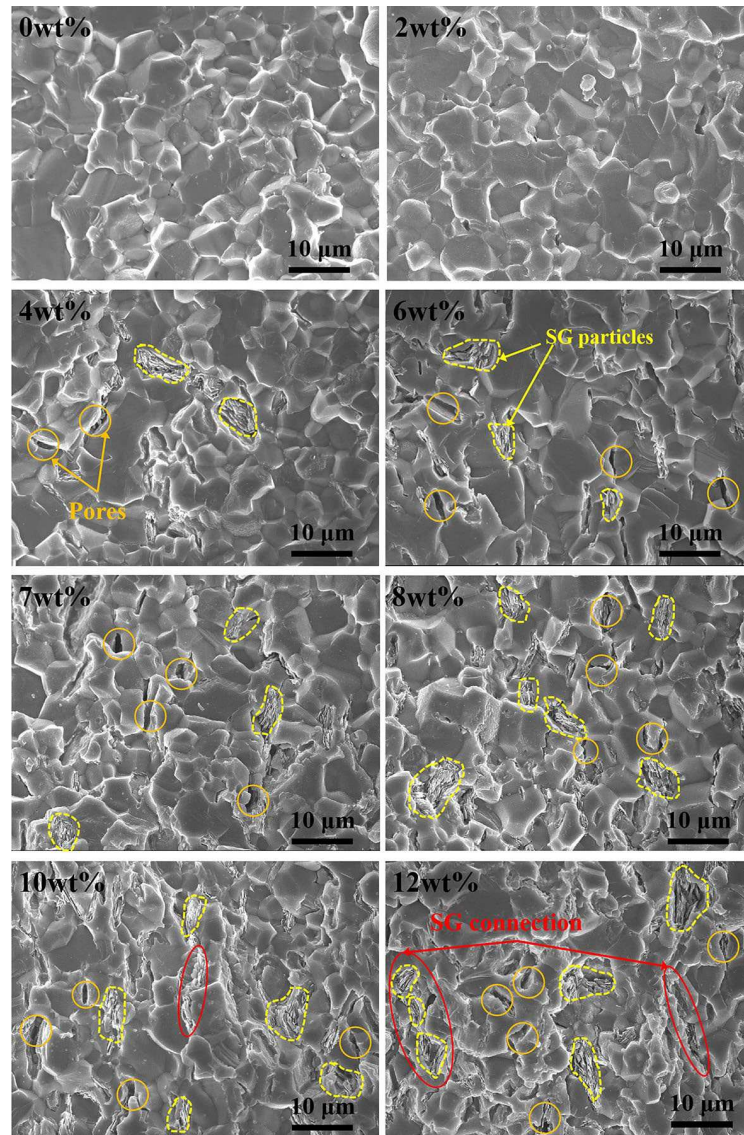


**Fig. 8 Fracture morphology of SG/AlN composites with different SG contents**

### 3.3 Mechanical Properties

To evaluate the mechanical properties of the SG/AlN composite ceramics, the flexural strength and fracture toughness of the SG/AlN composite as a function of SG content were obtained and shown in Figure 9. The strength of the composites decreases monotonically from 358 MPa to 240 MPa as the amount of SG increases from 0 wt% to 12 wt%, indicating that the addition of SG causes damage to the flexural strength of the composite. According to the fracture morphology analysis, the decrease in the strength

is mainly caused by the increasing number of pores in the composite and the weakening of the interfacial bonding between the SG particles and AlN matrix as more SG is incorporated into the composite, which greatly reduce the energy required for crack propagation during the fracture process.

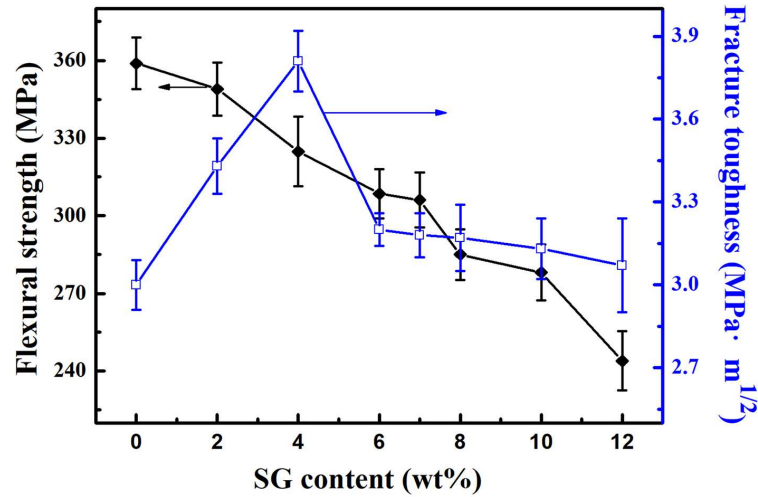


**Fig. 9 Mechanical properties of SG/AlN composites with different SG contents**

The fracture toughness of the composites exhibits an increasing trend at first and then decreases as the SG increases, reaching the maximum of 3.8 MPa·m<sup>1/2</sup> at 4 wt% SG, which is 27 % more than that of the monolithic AlN ceramic, revealing that a moderate addition of SG has a certain toughening effect on the SG/AlN composites. Fracture toughness is the ability of a material to resist crack propagation, and the main toughening mechanism that occurs in the SG/AlN composites can be determined through the SEM images of the fracture morphology. As shown in Figure 8, SG particles are dispersed homogeneously inside the composites, and composites with low SG content exhibit a high densification, which endows a strong interfacial bonding force between the SG particles and the AlN matrix. The high-resolution fracture morphology of the sample with 4 wt% SG after ultrasonic cleaning and without ultrasonic cleaning

are presented in Figures 10(a) and (b), respectively. As visible in Figure 10(a), the SG particles are tightly pinned inside the AlN grains, which induce a pinning effect in the material and consequently promote crack deflection during the crack propagation stage. In addition, the Figure 10(b) reveals that there are numerous extracted SG particles on the fracture surface, which is mainly because the SG particles were slightly deformed during the sintering process and became non-equiaxed particles. Considering the behavior of composite ceramics toughened by non-equiaxed materials such as graphene, carbon fibers, and CNTs [8], the extracted SG implies that numerous SG bridging and pulling-out have been generated during the fracture process, thus consuming a large quantity of fracture energy. This phenomenon reasonably toughens the SG/AlN composites. However, at higher SG contents, the increasing pores and the consequent decrease in density weaken the interfacial bonding between the AlN grains and SG particles, which has a significant and detrimental effect on the mechanical properties of the composite. As a result, a decreased fracture toughness is observed when the SG content exceeds 4 wt%.

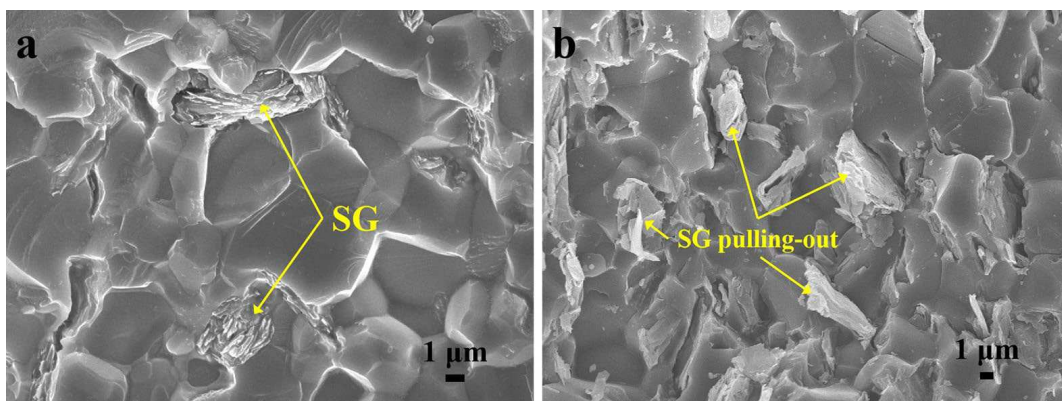


**Fig. 10 High-resolution fracture morphology of 4 wt% SG/AlN composite, (a) ultrasonic cleaning, (b) without ultrasonic cleaning**

### 3.4 Thermal Properties

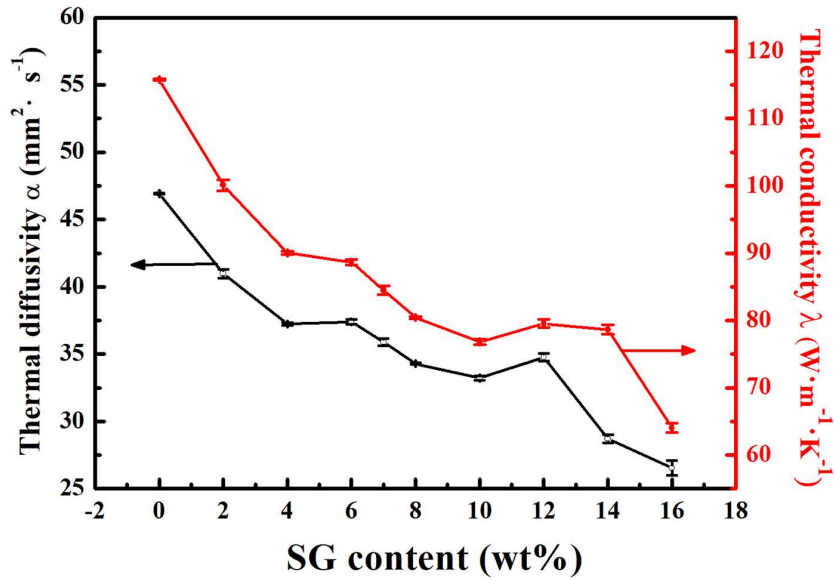


**Fig. 11 Thermal diffusivity  $\alpha$  and thermal conductivity  $\lambda$  of SG/AlN composites with different SG contents**

To investigate the thermal properties of the SG/AlN-base composites, the thermal diffusivity  $\alpha$  and thermal conductivity  $\lambda$  of the SG/AlN composite ceramics with varying SG contents were measured and are presented in Figure 11. Generally, both the  $\alpha$  and  $\lambda$  values of the composite ceramics exhibit a remarkable downtrend as the SG content increases from 0 to 16 wt%. The  $\alpha$  and  $\lambda$  of monolithic AlN ceramic are  $46.93 \text{ mm}^2 \cdot \text{s}^{-1}$  and  $115 \text{ W} \cdot \text{m}^{-1} \cdot \text{K}^{-1}$ , respectively. The  $\alpha$  of the composite with an SG content of 6, 7, 8, and 10 wt% is 37.41, 35.9, 34.30, and 33.22  $\text{mm}^2 \cdot \text{s}^{-1}$ , respectively, while the  $\lambda$  of the composite with an SG content of 6, 7, 8, and 10 wt% is 88.65, 84.5, 80.44, and 76.82  $\text{W} \cdot \text{m}^{-1} \cdot \text{K}^{-1}$ , respectively. These reveal that the addition of SG is detrimental to the thermal properties of the SG/AlN composites. Surprisingly, the  $\alpha$  and  $\lambda$  of the composite with 12 wt% SG exhibit an increase to  $34.76 \text{ mm}^2 \cdot \text{s}^{-1}$  and  $79.53 \text{ W} \cdot \text{m}^{-1} \cdot \text{K}^{-1}$ , respectively, instead of decrements. Further addition of SG to 16 wt% leads to the minimum  $\alpha$  and  $\lambda$

values of  $26.54 \text{ mm}^2 \cdot \text{s}^{-1}$  and  $64.04 \text{ W} \cdot \text{m}^{-1} \cdot \text{k}^{-1}$ , respectively.

As a covalently bonded inorganic compound, the  $\lambda$  of AlN crystals is strongly associated with phonon heat conduction [53], as described by the following Equation [54]:

$$\lambda = 1/3 cvl \quad (2)$$

where  $c$  is specific heat capacity,  $v$  is the mean velocity of the phonon, and  $l$  refers to the mean free path of the phonon. Enhanced phonon scattering results in the decrease of  $l$ , thereby reducing  $\lambda$  [53]. The phonon scattering in AlN-based composites mainly originates from various defect-phonon scattering, such as vacancies, dislocations, grain boundary interfaces, and pores [7]. For the SG/AlN composites, the growing SG/AlN interface as the SG addition enhances the phonons scattering and generates more interfacial thermal resistance, thus inducing a negative effect on the  $\lambda$  of the composites [8,54,55]. In addition, as the sources of scattering, the increasing number of pores at higher SG contents also contributes to the decrease in  $\lambda$ . The effect of porosity on  $\lambda$  of a material can be expressed as follows [56]:

$$\lambda = \lambda_0(1 - 3/2 \Phi) \quad (3)$$

where  $\lambda_0$  represents the thermal conductivity of a dense material, and  $\Phi$  is the porosity. Equation (3) shows that  $\lambda$  has an inverse relationship with the  $\Phi$  of a material, hence, the increasing pores as the SG addition also contribute a lot to the degradation of the  $\lambda$  of the SG/AlN composites. The abnormal increase in  $\lambda$  at 12 wt% SG may be ascribed to the formation of partial thermal-conduction paths caused by the connection of SG particles at higher SG contents. However, the further addition of SG seriously decreases

the densification and increases the number of pores in the composites, thus resulting in a dramatic decrease in the  $\lambda$  value to  $64.04 \text{ W}\cdot\text{m}^{-1}\cdot\text{k}^{-1}$  at 16 wt% SG.

In comparison with other AlN-based attenuating ceramics, the thermal properties of AlN-based composites containing different attenuating agents are tabulated in Table 1. Generally, the  $\lambda$  of the SG/AlN composites are significantly higher than that of AlN/SiC attenuating composite ceramics ( $40$  to  $70 \text{ W}\cdot\text{m}^{-1}\cdot\text{k}^{-1}$ , [1,10,11]) at the same content of the second phase. Simultaneously, in comparison to the AlN-based composites containing 1/2D carbon materials, such as graphene and carbon nanotubes, as the second phase [7–9], at the same content, the SG/AlN composite shows a relatively higher  $\lambda$  as well. For example, the  $\lambda$  of the AlN/graphene composite containing 0.1 vol% (0.07 wt%) graphene prepared by Simsek et al. [7] is only  $74 \text{ W}\cdot\text{m}^{-1}\cdot\text{k}^{-1}$  in the direction parallel to the graphene plane, and that of the 10 vol% (7 wt%) graphene nanosheet/AlN composite reported by Yun et al. [8] is as low as  $40 \text{ W}\cdot\text{m}^{-1}\cdot\text{k}^{-1}$ . Similarly, carbon nanotubes have been reported to have a thermal conductivity up to  $6600 \text{ W}\cdot\text{m}^{-1}\cdot\text{k}^{-1}$ , whereas the AlN/CNT composite with 6 vol% (4 wt%) CNTs shows a relatively low  $\lambda$  of  $62 \text{ W}\cdot\text{m}^{-1}\cdot\text{k}^{-1}$  [9]. All of these values are lower than the  $\lambda$  value of SG/AlN composite with 10 wt% SG prepared in this study at  $76.82 \text{ W}\cdot\text{m}^{-1}\cdot\text{k}^{-1}$ , indicating that SG had the least impact on the  $\lambda$  of AlN-based composites relative to other types of attenuating agents, which is credited to its spherical morphology. Similarly, Ren et al. [57] found that the thermal conductivity of spherical BN/PDMS composites ( $2.30 \text{ W}\cdot\text{m}^{-1}\cdot\text{k}^{-1}$ ) is almost four times higher than that of platelet-like BN/PDMS composites ( $0.60 \text{ W}\cdot\text{m}^{-1}\cdot\text{k}^{-1}$ ). It is mainly because the spherical filler can not only reduce the interface

thermal resistance and phonon scattering compared with platelet-like one, but also decrease the BN agglomeration and thus greatly promotes heat conduction.

As schematically shown in Figures 12(a) and (b), compared to the flake-shaped heterogeneous interface of AlN-based composites containing 2D flake graphite, ideally, the SG/AlN interface surrounding the SG should also be a spherical morphology, which endows a remarkably lower cross-sectional area for the heterogeneous interface in the direction of thermal conduction. Additionally, in comparison with graphene, CNTs, and other 1D/2D attenuating agents incorporated at the same volume fraction, the addition of SG shows a slightly inhibited effect of the AlN grains. Zhang et al. [25] reported that the larger the particle size is, the lower the thermal conductive barrier it provides. It can be inferred that the relatively larger AlN grains due to the addition of SG extremely lessen the conductive barrier, this is in great contrast with the sharp decrease in the  $\lambda$  of graphene/AlN composites as the AlN particle size decreases [8,23,60]. All the above factors can considerably diminish the interfacial thermal resistance of the SG/AlN composites. The effect of interfacial thermal resistance on heat conduction can be given by the Formula (4) [61]:

$$Q_i = \Delta T / R_i \quad (4)$$

where  $Q_i$  represents the value of the heat flux at interface,  $\Delta T$  is temperature difference at interface, and  $R_i$  is interfacial thermal resistance. It can be deduced that the lower interfacial thermal resistance delivers a higher heat flux through the interface. Consequently, the SG/AlN composites with a lower interfacial thermal resistance exhibit a significantly improved heat-conduction ability.

**Table 1 Thermal properties of AlN-based composites with different second phases**

Samples	Sintering method	Purity of raw AlN powder	AlN grain size ( $\mu\text{m}$ )	Second phase content	Thermal diffusivity ( $\text{mm}^2 \cdot \text{s}^{-1}$ )	Thermal conductivity ( $\text{W} \cdot \text{m}^{-1} \cdot \text{K}^{-1}$ )	Refs.
Graphene Nanosheet/AlN	Hot-pressing	97.70 %	$\leq 3.5$	10 vol%		35.9 (Through-plane)	[8]
SWCNT/AlN	Hot-pressing	97.99 %	2	6 vol%		62	[9]
SiC/AlN	Plasma activated sintering	99.99 %	3	10 wt%	15	36	[11]
Graphene platelets/AlN	Spark plasma sintering	99.90 %	$1.73 \pm 0.02$	9.5 wt%	4.64	19.8	[23]
SiC/AlN	Hot-pressing	98.50 %	-	10 wt%		65	[58]
Graphene/AlN	Hot-pressing	97.99 %	6	10 wt%	18.95	39.7 (Through-plane)	[59]
Graphene platelets/AlN	Spark plasma sintering	$\leq 99.22$ %	$2 \pm 1.4$	8 wt%	19	43 (Through-plane)	[60]
					37	84 (In-plane)	
Spherical graphite/AlN	Hot-pressing	99.90 %	$\sim 7$	10 wt%	33.22	76.8 (Through-plane)	This work

On the other side, since SG has a low-anisotropic  $\lambda$ , as distinguished from that of 2D materials with a uniaxially high  $\lambda$ , regardless of directions, there should be two thermally conductive paths within the SG/AlN composites. As indicated by the yellow arrow in Figure 12(a), one is the SG-AlN thermally conductive path, and another is the AlN matrix thermally conductive path, both of which hugely promotes the  $\lambda$  of the SG/AlN composites. The synergistic effect of the reduced interfacial thermal resistance and the low-anisotropic thermal conductivity of SG can deliver a higher  $\lambda$  for the SG/AlN composites. Moreover, the issue of the anisotropic  $\lambda$  for the composites containing 1/2D carbonaceous materials can also be alleviated by the weak orientation alignment of SG, further evidencing the potential of applying SG in the preparation of

highly thermally conductive microwave attenuating materials with low anisotropy.

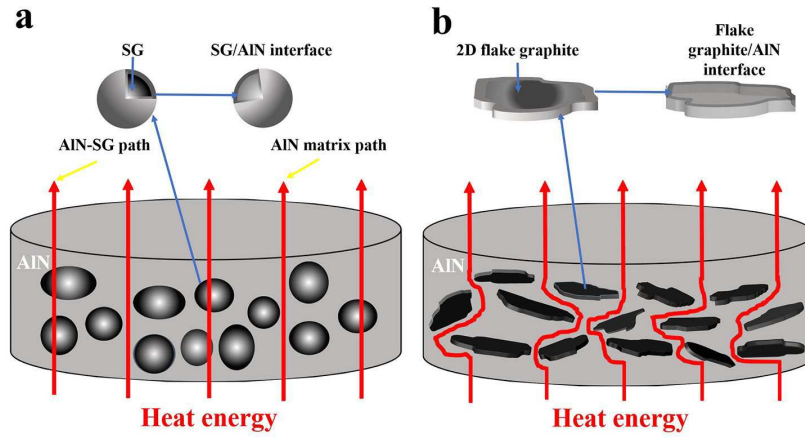


**Fig. 12** The schematic diagram of thermally conductive path in composite filled with different shaped second phase, (a) spherical graphite, (b) 2D flake graphite

### 3.5 Dielectric Properties

The microwave absorption performance of a non-magnetic absorption material is strongly dependent on its dielectric properties, such as the real dielectric constant  $\epsilon'$ , imaginary dielectric constant  $\epsilon''$ , and dielectric loss. The real and imaginary part of the dielectric constant refers to the polarization and lossy ability of the material under an applied electromagnetic field, respectively, and the dielectric loss is reflected by the loss tangent ( $\tan \delta = \epsilon''/\epsilon'$ ) [62]. The dielectric constant and dielectric loss as a function of microwave frequency (8.2 to 12.4 GHz) of the SG/AlN composites with different SG contents are depicted in Figures 13 and 14, respectively. Both the dielectric constant and dielectric loss of the composites show a significant increment as the SG content increases from 0 wt% to 8 wt%. The  $\epsilon'$ ,  $\epsilon''$ , and  $\tan \delta$  values of the monolithic AlN ceramic are 8.3 to 8.7, 0.03 to 0.07, and 0.004 to 0.008, respectively, showing an extremely low dielectric loss. While the  $\epsilon'$ ,  $\epsilon''$  and  $\tan \delta$  values for the 8 wt% composite

are 50 to 64, 30 to 32 and 0.46 to 0.59, respectively, implying that the addition of SG has a pronounced improved effect on the dielectric loss of the SG/AlN composite materials.

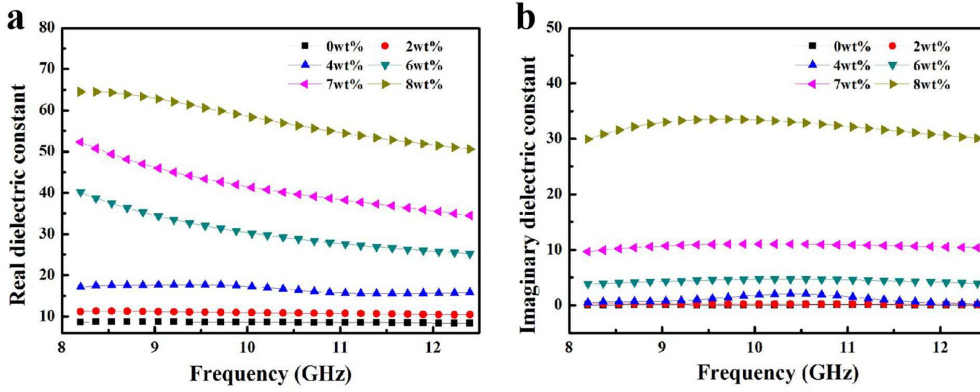


Fig. 13 Dielectric constant of SG/AlN composites with different SG contents

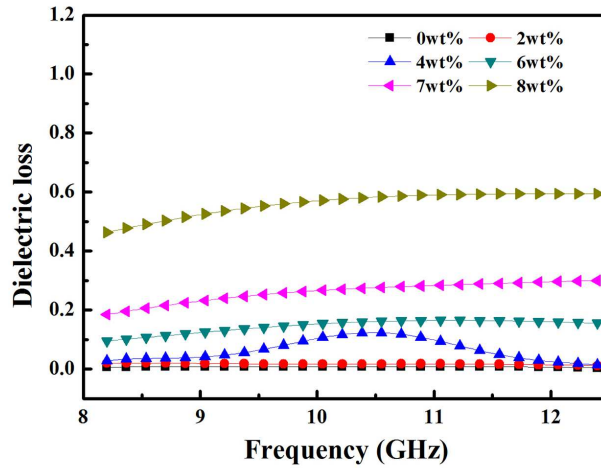


Fig. 14 Dielectric loss of SG/AlN composites with different SG contents

The real dielectric constant  $\epsilon'$ , which reflects the polarization ability of the material, is closely linked with the ability of the material to store charges [63], and it is given by Equation (5) [62]:

$$\epsilon' = \frac{\epsilon_s - \epsilon_\infty}{1 + \omega^2 \tau^2} + \epsilon_\infty \quad (5)$$

where  $\epsilon_s$  is the static dielectric constant,  $\epsilon_\infty$  is the optical dielectric constant,  $\tau$  is the

polarization relaxation time, and  $\omega$  is the angular frequency. Inside the insulating AlN matrix, the conductive phase, the SG particles, act as electrode plates and readily create a mini-capacitor effect. The shorter the distance between conductive SG particles, the further improved the capacitance of the composites, that is, the enhanced mini-capacitor effect. From this, the ability of the composites to store charges is sufficiently improved and in turn enhances the  $\epsilon'$  value. The  $\epsilon''$  value can be calculated using the following Equation (6) [63,64]:

$$\epsilon'' = \frac{\sigma}{\omega\epsilon_0} + \frac{\epsilon_s - \epsilon_\infty}{1 + \omega^2\tau^2} \omega\tau = \epsilon_c + \epsilon_{\text{relax}} \quad (6)$$

where  $\sigma$  is the electrical conductivity of the material,  $\epsilon_0$  is the dielectric constant of free space ( $8.854 \times 10^{-12} \text{ F}\cdot\text{m}^{-1}$ ) [62],  $\epsilon_c$  and  $\epsilon_{\text{relax}}$  are the conduction loss and Debye relaxation loss, respectively. The imaginary part of the dielectric constant is proportional to the conductivity of the material, that is, conduction loss. As the conductive phase SG is incorporated into the matrix, it gradually forms a three-dimensional conductive network, which then significantly increases the electrical conductivity of the composite material and the electronic migration on the surface of the SG particles increases significantly, thereby enhancing the conduction loss of the material. It can be deduced from Equations (5) and (6) that the  $\epsilon'$  and  $\epsilon''$  values of the materials are closely related to the Debye relaxation loss. Based on the Debye theory, if there is no consideration of the influence of conduction loss on the  $\epsilon''$  value, the Debye relaxation loss can be deduced from the by  $\epsilon''$ - $\epsilon'$  curve, and the relationship between the real and imaginary parts of the dielectric constant can be described as follow [65]:

$$(\varepsilon'')^2 + \left(\varepsilon' - \frac{\varepsilon_s + \varepsilon_\infty}{2}\right)^2 = \left(\frac{\varepsilon_s - \varepsilon_\infty}{2}\right)^2 \quad (7)$$

If there is a polarization relaxation behavior existing in the material, a semicircle occurs in the  $\varepsilon''$ - $\varepsilon'$  curve, which is called the Cole-Cole semicircle [65]. The  $\varepsilon''$  dependent  $\varepsilon'$  curves of the SG/AlN composites with varying SG contents are displayed in Figure 15. No obvious semicircle is observed in the curves of the 0 wt% and 2 wt% SG samples, while the samples containing 4, 6, 7 and 8 wt% SG exhibit an identifiable Cole-Cole semicircle. This indicates that the SG addition leads to an obvious polarization relaxation behavior in the composite, which should be attributed to the synergistic effect of SG particle, AlN grains and SG/AlN heterogeneous interfaces.

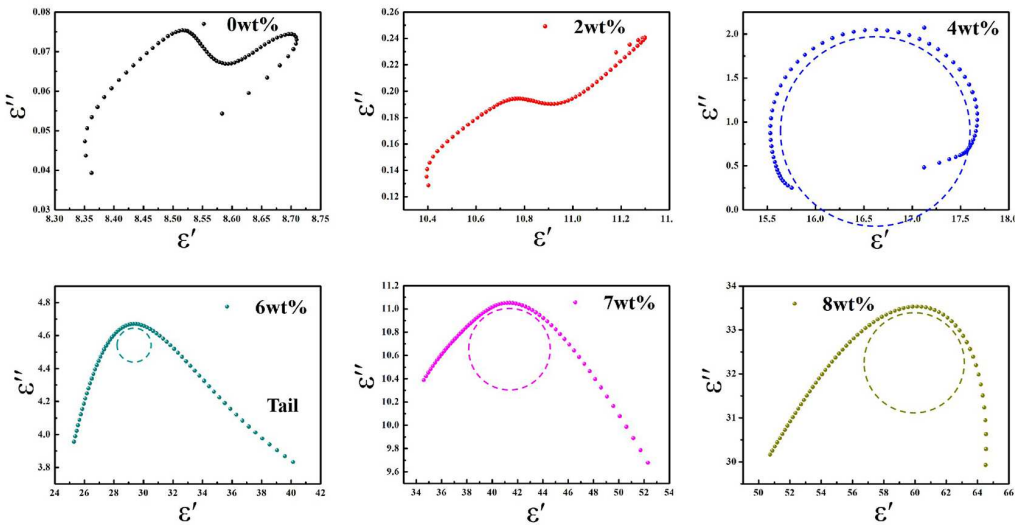


**Fig. 15 The  $\varepsilon'$ - $\varepsilon''$  curves of SG/AlN composites with different SG contents**

In the SG/AlN composites, the electronic transport in the SG-SG micro-capacitors is mainly realized via insulated AlN matrix, and the insulated AlN is equivalent to a tunneling resistance. The evenly dispersing SG in the AlN matrix means that the SG-SG micro-capacitors and AlN grain resistance will form repeated polarizations inside the material. In addition, owing to the large mismatch between the electrical conductivity of

AlN and SG, the space charge polarization was strongly built as a result of the charge accumulation at the SG/AlN heterogeneous interfaces, which can also be considered a micro-capacitor. In this regard, the dielectric properties of SG/AlN composites can be expressed by the equivalent circuit. To have a better understanding of the effect of the addition of SG on the dielectric properties of the composites, the AC impedance of the 2-8 wt% composites were tested and the relevant impedance spectrum are shown in Figure 16(a-e). Combined with software analysis and repeated tests, the equivalent circuit that mostly fits the micro-region in the composites is schematically shown in Figure 16(f), wherein the red curves in Figures 16(a-e) are the fitting curves deserved from the equivalent circuit. The impedance ( $Z$ ) corresponding to the equivalent circuit can be given by Equation (8):

$$\frac{1}{Z} = \frac{1}{R + 1/i\omega C_1} + \frac{1}{1/i\omega C_2} \quad (8)$$

where  $C_1$  represents SG-SG micro-capacitor,  $C_2$  represents the micro-capacitor corresponding to the space charge polarization,  $R$  represents the tunneling resistance of AlN grain. The  $R$ ,  $C_1$  and  $C_2$  values of the equivalent circuit of the SG/AlN composites with different SG content are presented in Table 2. Notably, the decreasing  $R$  indicating that the conductivity of the composites was significantly improved by the SG addition. In contrast, the  $C_1$  and  $C_2$  exhibit a monotonous increase with the elevated SG content, which suggests that more micro-capacitor structures and space charge polarization are generated inside the material. These further demonstrates that the improved conductivity and the polarization relaxation composed of SG-SG micro-capacitors, AlN grain resistance and SG/AlN heterogeneous interfaces resulting from the SG addition

contribute a lot to the enhancement of the  $\epsilon'$  and  $\epsilon''$  values. Whereas, aside from the typical Cole-Cole semicircle, a smooth tail is also observed in the  $\epsilon''$ - $\epsilon'$  curves for the samples with 6–8 wt% SG, which may be attributed to that the excessive conduction loss caused by the SG addition hides the effect of the relaxation process, the similar results can also be found in earlier reports [65-67]. Accordingly, in parallel with the variation of the real and imaginary dielectric constants, the loss tangent  $\tan \delta$  determined by  $\epsilon'$  and  $\epsilon''$  also exhibits an improvement, suggesting that the addition of SG enhances the dielectric loss capability of the composite.

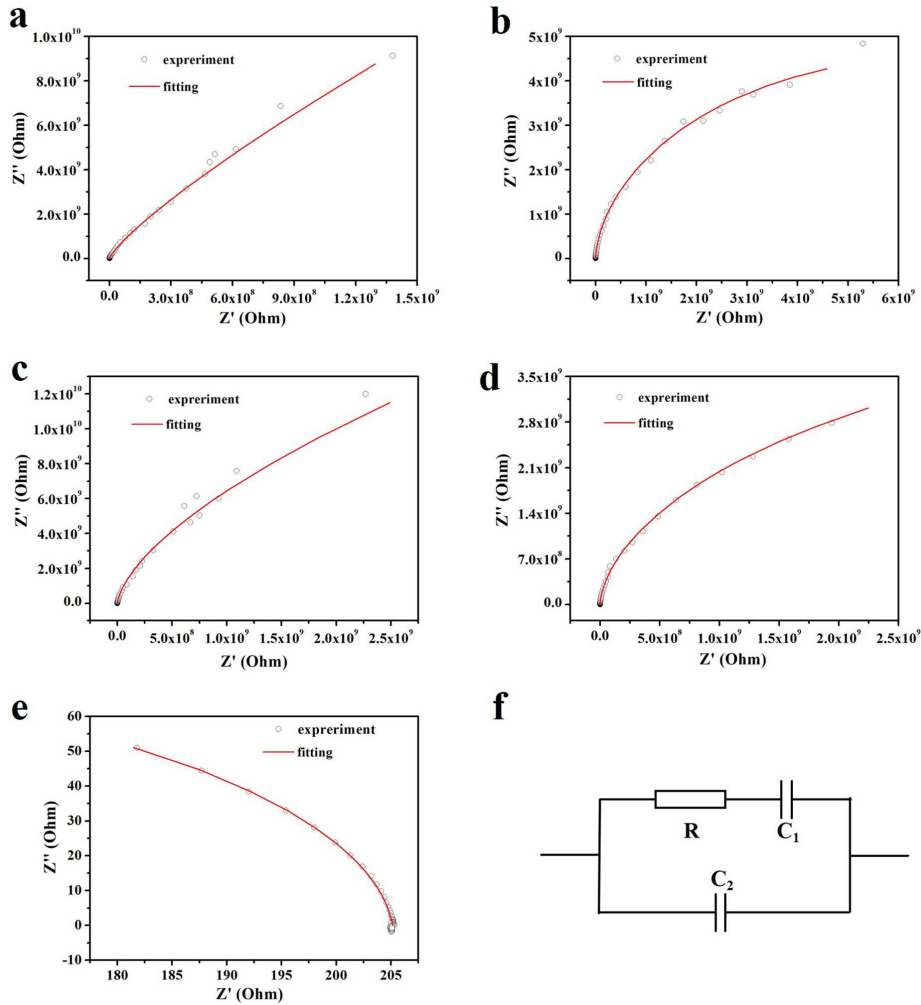


**Fig. 16** The impedance spectrum of the SG/AlN composites (a) 2 wt%, (b) 4 wt%, (c) 6 wt%, (d) 7 wt%, (e) 8 wt%, and (f) equivalent circuit model of a micro-region in the composites

**Table 2 Modeled parameters of the equivalent circuit model in the SG/AlN composites**

SG content (wt %)	R	C <sub>1</sub>	C <sub>2</sub>
2	1.623×10 <sup>10</sup>	1.038×10 <sup>-11</sup>	3.641×10 <sup>-12</sup>
4	6.433×10 <sup>9</sup>	4.681×10 <sup>-11</sup>	1.15×10 <sup>-11</sup>
6	5.208×10 <sup>9</sup>	8.308×10 <sup>-11</sup>	1.291×10 <sup>-11</sup>
7	4.578×10 <sup>9</sup>	1.077×10 <sup>-10</sup>	2.243×10 <sup>-11</sup>
8	205.5	9.45×10 <sup>-9</sup>	8.423×10 <sup>-10</sup>

### 3.6 Microwave Absorption Properties

The microwave absorption property of material is usually characterized by the reflection loss (RL), which is expressed according to Equation (9) [68,69]:

$$RL = 20 \lg \left| \frac{Z_{in} - Z_0}{Z_{in} + Z_0} \right| \quad (9)$$

where  $Z_0$  is the impedance in free space, and  $Z_{in}$  is the incident impedance of the material surface, which can be obtained from Equation (10) [68,69]:

$$Z_{in} = Z_0 \sqrt{\frac{\mu_r}{\epsilon_r}} \tanh \left[ j \frac{2\pi}{c} \sqrt{\mu_r \epsilon_r} f d \right] \quad (10)$$

where  $f$  refers to the frequency of the electromagnetic wave,  $c$  is the speed of light ( $3 \times 10^8$  m/s),  $d$  denotes the material thickness, and  $\epsilon_r$  and  $\mu_r$  are the complex permittivity and complex permeability of the material, respectively (for non-magnetic materials,  $\mu_r$  is commonly set to 1) [70]. RL is generally a negative value, and the smaller the value is, the stronger the absorption ability of the material. For instance, RL values below -4 dB and -10 dB means that the material can absorb 36 % and 90 % of electromagnetic wave, respectively, and the latter case is considered as an effective absorption [68]. Figure 17 shows the RL of the SG/AlN composites as a function of SG contents at the thickness of 1 mm. In the X-band, as the SG content increases from 0 wt% to 8 wt%, the  $RL_{\min}$  of the composites gradually decreases first, and then increases. When the SG content is

less than 6 wt%, all the  $RL_{\min}$  values are higher than -4 dB, indicating a poor absorption capability for electromagnetic waves. The RL value of 7 wt% sample significantly decreases with the increasing frequency in the X-band, and it shows the best absorption performance with a  $RL_{\min}$  value of -14 dB at 12.4 GHz. In comparison, the SiC/AlN composites prepared by Li et al. [11] exhibited a optimized absorption ability with the  $RL_{\min}$  of -16.5 dB at 30 wt% SiC, while its thermal conductivity ( $24.88 \text{ W}\cdot\text{m}^{-1}\cdot\text{k}^{-1}$ ) is significantly lower than that of 7 wt% SG/AlN composite ( $84.5 \text{ W}\cdot\text{m}^{-1}\cdot\text{k}^{-1}$ ). This shows a integrated strong attenuation and high thermal conductivity can be obtained by SG/AlN composites.

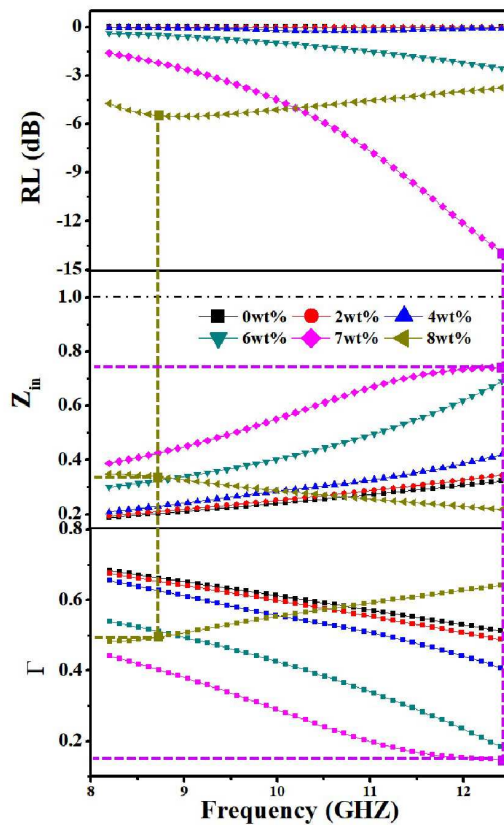


**Fig. 17 Reflection loss, incident impedance and reflection coefficient of SG/AlN composites with different SG contents**

The improved absorption ability of the sample should be attributed to the enhanced

dielectric loss, which is mainly derived from the interfacial polarization loss and conduction loss as a result of the addition of SG. Additionally, the improved charge storage ability resulting from the enhanced mini-capacitor effect also boosts the microwave absorption of the materials.

Despite the  $RL_{\min}$  and best effective absorbing bandwidth (EAB,  $\leq -10$  dB) of -13.9 dB and 0.87 GHz, respectively, occurring for the 7 wt% SG sample, its overall absorption performance is not as satisfactory as enough. And further increasing the SG content to 8 wt% deteriorates the microwave absorption ability of the composite, with a  $RL_{\min}$  value of -5.5 dB. This is attributed to the impedance mismatch caused by the high dielectric constant of the composites. Excellent absorption materials should have, apart from a great loss ability for electromagnetic waves, a good impedance matching characteristic to reduce the reflection of electromagnetic waves on the surface of the material [65]. The ability of reflecting electromagnetic waves and the impedance matching characteristic of a material can be expressed by reflection coefficient  $\Gamma$  [71]:

$$\Gamma = |(Z_{in} - Z_0) / (Z_{in} + Z_0)| \quad (11)$$

A low  $\Gamma$  value supports a good impedance matching, that is, more electromagnetic waves could enter the material. The free-space impedance  $Z_0$  value is fixed at 1, thus, it can be speculated from Equation (11) that a low  $\Gamma$  value, i.e., a well-matched impedance, can be obtained when the  $Z_{in}$  value is close to 1 [72]. To obtain a deeper understanding of the absorption ability of the SG/AlN composites, the calculated  $Z_{in}$  and  $\Gamma$  values as a function of SG content are illustrated in Figure 17. It can be seen from the  $RL$ ,  $Z_{in}$ , and  $\Gamma$  curves of the 7 wt% and 8 wt% samples that at the frequency with the maximum  $Z_{in}$

value (closest to 1), the materials exhibit the smallest  $\Gamma$  value. This indicates the  $RL_{\min}$  value can be achieved at the best impedance matching, i.e., when there is the least reflection of electromagnetic waves. Overall, the  $Z_{in}$  values of all the SG/AlN composites are within in the range of 0 to 1 in the X-band, and they increase first and then decrease as the SG content increases from 0 wt% to 8 wt%, reaching the maximum at 7 wt% SG. Conversely, the reflection coefficient  $\Gamma$  of the composites gradually decreases as more SG is incorporated, attaining the minimum at 7 wt% SG (0.14 to 0.44), indicating the best impedance matching in the composite with 7 wt% SG, which is in good agreement with its absorption ability. The above results indicate that a good impedance is critical to the achievement of an excellent absorption property, which is highly dependent on the SG content. However, despite a high dielectric loss ability at a high SG content (8 wt%), the sample exhibits a weak absorption capability as a result of its poor impedance matching. On the whole, the AlN-based microwave attenuating composite ceramics, with its combined high thermal conductivity, improved dielectric loss, enhanced absorption ability and low anisotropy, are developed by employing SG as attenuating agent.

#### **4 Conclusion**

In this work, SG/AlN microwave attenuating composite ceramics with 0 to 16 wt% spherical graphite (SG) as the attenuating agent were prepared via hot-pressing sintering. The SG particles are homogeneously dispersed in the sintered bodies, displaying a three-dimensional morphology and a negligible orientation alignment. The addition of SG impedes the sintering of the composites, while slightly influences on the growth of

AlN grains. As the amount of SG added increases, the strength of the composites decreases monotonously, while the toughness initially increases and then decreases, with the maximum at  $3.8 \text{ MPa}\cdot\text{m}^{1/2}$  for the composite with 4 wt% SG, demonstrating a moderate toughening effect. Despite the significant decrease in the thermal conductivity with SG addition, the SG/AlN composites exhibit a relatively higher thermal conductivity compared to other composites with non-spherical attenuating agents. The enhanced polarization loss, conduction loss, and mini-capacitor effect with the addition of SG (0 wt% to 8 wt%) significantly improve the dielectric constant and loss (0.004–0.008 to 0.46–0.59) of the composites within the frequency range of 8.2 GHz to 12.4 GHz. The absorption ability is enhanced as SG is added, with composite with 7 wt% SG having the best absorption performance with an  $RL_{\min}$  of -14 dB at 12.4 GHz) and a wide EAB (0.87 GHz) at 7 wt% composite. In summary, the as-prepared SG/AlN composites are promising low anisotropic and highly thermally conductive attenuating materials.

### **Acknowledgement**

This work was supported by the Priority Academic Program Development of Jiangsu Higher Education Institutions (PAPD), the Postgraduate Research&Practice Innovation Pro-gram of Jiangsu Province (KYCX20\_0990), Qing Lan Project, the Program for Changjiang Scholars, Innovative Research Team in University (PCSIRT), IRT1146 and IRT15R35, and the Top-notch Academic Programs Project of Jiangsu Higher Education Institutions (TAPP, PPZY2015B128).

### **References**

- [1] Zang XR, Lu YP. Preparation and dielectric properties at high frequency of AlN-based composited ceramic. *J Mater Sci: Mater Electron* 2020, **31**: 2826–2832.
- [2] Chen CF, Perisse ME, Ramirez AF, et al. Effect of grain boundary phase on the thermal conductivity of aluminium nitride ceramics. *J Mater Sci* 1994, **29**: 1595–1600.
- [3] Mikijelj B, Abe DK, Hutcheon R. AlN-based lossy ceramics for high average power microwave devices: performance-property correlation. *J Eur Ceram Soc* 2003, **23**: 2705–2709.
- [4] Calame JP, Abe DK, Levush B, et al. Variable temperature measurements of the complex dielectric permittivity of lossy AlN-SiC composites from 26.5–40 GHz. *J Appl Phys* 2001, **89**: 5618.
- [5] Chen YM, Pang L, Li Y, et al. Ultra-thin and highly flexible cellulose nanofiber/silver nanowire conductive paper for effective electromagnetic interference shielding. *Composites, Part A* 2020, **135**: 105960.
- [6] Green M, Chen XB. Recent progress of nanomaterials for microwave absorption. *J Electroceramics* 2019, **5**: 503–541.
- [7] Simsek ING, Andrés N, Eugenio G, et al. The effect of graphene nanoplatelets on the thermal and electrical properties of aluminum nitride ceramics. *J Eur Ceram Soc* 2017, **37**: 3721–3729.
- [8] Yun C, Feng YB, Qiu T, et al. Mechanical, electrical, and thermal properties of graphene nanosheet/aluminum nitride composites. *Ceram Int* 2015, **41**: 8643–8649.
- [9] Chakravarty A, Singh R, Roy S, et al. Aluminum nitride-single walled carbon nanotube nanocomposite with superior electrical and thermal conductivities. *J Am Ceram Soc* 2017, **100**: 3360–3364.
- [10] Gu JL, Sang LL, Pan B, et al. Thermal conductivity and high-frequency dielectric properties of pressureless sintered SiC-AlN multiphase ceramics. *Mater* 2018, **11**: 969.
- [11] Li PW, Wang CB, Liu HX, et al. Structural, thermal and dielectric properties of AlN–SiC composites fabricated by plasma activated sintering. *Adv Appl Ceram*

- 2019, **118**: 313–320.
- [12] Chakravarty A, Singh R, Roy S, et al. Enhanced microwave absorption performance of double-layer absorbers containing BaFe<sub>12</sub>O<sub>19</sub> ferrite and graphite nanosheet composites. *J Electron Mater* 2017, **100**: 3360–3364.
- [13] Meng R, Zhang T, Yu HJ, et al. A facile coprecipitation method to Fe<sub>x</sub>O<sub>y</sub>/Fe decorated graphite sheets with enhanced microwave absorption properties. *Nanotechnol* 2019, 185704
- [14] Qiu J, Qiu T. Fabrication and microwave absorption properties of magnetite nanoparticle-carbon nanotube-hollow carbon fiber composites. *Carbon* 2015, **81**: 20–28.
- [15] Gupta KK, Abbas SM, Abhyankar AC. Carbon black/polyurethane nanocomposite-coated fabric for microwave attenuation in X & Ku-band (8-18 GHz) frequency range. *J Ind Text* 2016, **46**: 510–529.
- [16] Kim JB, Lee SK, Kim CG. Comparison study on the effect of carbon nano materials for single-layer microwave absorbers in X-band. *Compos Sci Technol* 2008, **68**: 2909–2916.
- [17] Meng FB, Wang HG, Huang F, et al. Graphene-based microwave absorbing composites: A review and prospective. *Composites, Part B* 2018, **137**: 260–277.
- [18] Liao XJ, Ye W, Chen LL, et al. Flexible hdC-G reinforced polyimide composites with high dielectric permittivity. *Composites, Part A* 2017, **101**: 50–58.
- [19] Xu WH, Ding YC, Yu Y, et al. Highly foldable PANi@CNTs/PU dielectric composites toward thin-film capacitor application. *Mater Lett* 2017, **192**: 25–28.
- [20] Liang HL, Wang CP, Huo YL, et al. AlN/CNT composites ceramics by spark plasma sintering. *Key Eng Mater* 2014, **603**: 570–573.
- [21] Shen Y, Zhang H, Yang AM, et al. Outgassing property of carbon nanotube cathode with intense pulsed emission. *Acta Phys Sin* 2012, **61**: 103–109.
- [22] Shen Y, Zhang H, Liu XG, et al. Outgassing mass spectrum analysis with intense pulsed emission of carbon nanotube cathode. *Acta Phys Sin* 2011, **60**: 080702.
- [23] Yin R, Zhang YB, Zhao W, et al. Graphene platelets/aluminium nitride metacomposites with double percolation property of thermal and electrical

- conductivity. *J Eur Ceram Soc* 2018, **38**: 4701–4706.
- [24] Chen JK, Wang LM, Gui XC, et al. Strong anisotropy in thermoelectric properties of CNT/PANI composites. *Carbon* 2017, **114**: 1–7.
- [25] Zhang XY, Shi ZQ, Zhang X, et al. Three dimensional AlN skeleton-reinforced highly oriented graphite flake composites with excellent mechanical and thermophysical properties. *Carbon* 2018, **131**: 94–101.
- [26] Fan YZ, Yang HB, Li MH, et al. Evaluation of the microwave absorption property of flake graphite. *Mater Chem Phys* 2009, **115**: 696–698.
- [27] Yuan GM, Li XK, Dong ZJ, et al. Graphite blocks with preferred orientation and high thermal conductivity. *Carbon* 2012, **50**: 175–182.
- [28] Zheng WE, Wong SC. Electrical conductivity and dielectric properties of PMMA/expanded graphite composites. *Compos Sci Technol* 2003, **63**: 225–235.
- [29] He F, Lau S, Chan HL, et al. High dielectric permittivity and low percolation threshold in nanocomposites based on poly (vinylidene fluoride) and exfoliated graphite nanoplates. *Adv Mater* 2009, **21**: 710–715.
- [30] Wang P, Cheng LF, Zhang Y, et al. Electrospinning of graphite/SiC hybrid nanowires with tunable dielectric and microwave absorption characteristics. *Composites, Part A* 2018, **104**: 68–80.
- [31] Du YC, Liu T, Yu B, et al. The electromagnetic properties and microwave absorption of mesoporous carbon. *Mater Chem Phys* 2012, **135**: 884–891.
- [32] Torğut G, Biryant F, Demirelli K. Effect of graphite particle fillers on dielectric and conductivity properties of poly (NIPAM-co-HEMA). *Bull Mater Sci* 2019, **42**: 244.
- [33] Sun MY, Bai YH, Li MX, et al. Improved toughness and electromagnetic shielding-effectiveness for graphite-doped SiC ceramics with a net-like structure. *J Eur Ceram Soc* 2018, **38**: 5271–5281.
- [34] Zhang Y, He PG, Yuan JK, et al. Effects of graphite on the mechanical and microwave absorption properties of geopolymer based composites. *Ceram Int* 2017, **43**: 2325–2332.
- [35] Kováčika J, Emmer Š. Cross property connection between the electric and the thermal conductivities of copper graphite composites. *Int J Eng Sci* 2019, **144**:

103130.

- [36] Marinopoulo AG, Reining L, Olevano V, et al. Anisotropy and interplane interactions in the dielectric response of graphite. *Phys Rev Lett* 2002, **89**: 076402.
- [37] Zeng FK, Xue C, Ma HB, et al. High thermal conductivity and anisotropy values of aligned graphite flakes/copper foil composites. *Mater* 2020, **13**: 46.
- [38] Li WJ, Liu Y, Wu GH. Preparation of graphite flakes/Al with preferred orientation and high thermal conductivity by squeeze casting. *Carbon* 2015, **95**: 545–551.
- [39] Yoshio M, Wang H, Fukuda K. Spherical carbon-coated natural graphite as a lithium-ion battery-anode material. *Angew Chem, Int Ed* 2003, **42**: 4203–4206.
- [40] Wu YS, Wang YH, Lee YH. Performance enhancement of spherical natural graphite by phenol resin in lithium ion batteries. *J Alloys Compd* 2006, **426**: 0–222.
- [41] Li M, Fang ZR, Wang SK, et al. Thermal conductivity enhancement and heat transport mechanism of carbon fiber z-pin graphite composite structures. *Compos* 2019, **172**: 603–611.
- [42] Huang D, Tian ZB, Cui W, et al. Effects of Y<sub>2</sub>O<sub>3</sub> and yttrium aluminates as sintering additives on the thermal conductivity of AlN ceramic substrates. *Ceram Int* 2018, **44**: 20556–20559.
- [43] Nakano H, Watari K, Hayashi H, et al. Microstructural characterization of high-thermal-conductivity aluminum nitride ceramic. *J Am Ceram Soc* 2002, **85**: 3093–3095.
- [44] Narang V, Korakakis D, Seehra MS. Electronic state of Er in sputtered AlN:Er films determined by magnetic measurements. *J Appl Phys* 2014, **116**: 213911.
- [45] Jiang SH, Cheong JY, Nam JS, et al. High-density fibrous polyimide sponges with superior mechanical and thermal properties. *ACS Appl Mater Interfaces* 2020, **12**: 19006–19014.
- [46] Wang F, Chen L, Li HL, et al. N-doped honeycomb-like porous carbon towards high-performance supercapacitor. *Chin Chem Lett* 2020, **56**: 3935–3938.
- [47] Yan DF, Guo L, Xie C, et al. N, P-dual doped carbon with trace Co and rich edge sites as highly efficient electrocatalyst for oxygen reduction reaction. *Sci China Mater* 2018, **61**: 679–685.

- [48] Zhao CL, Wu YX, Liang HL, et al. N-doped graphene and TiO<sub>2</sub> supported manganese and cerium oxides on low-temperature selective catalytic reduction of NO<sub>x</sub> with NH<sub>3</sub>. *J Adv Ceram* 2018, **7**: 197–206.
- [49] Zhou SZ, Zhou GY, Jiang SH, et al. Flexible and refractory tantalum carbide-carbon electrospun nanofibers with high modulus and electric conductivity. *Mater Lett* 2017, **200**: 97–100.
- [50] Kuang B, Song WL, Ning MQ, et al. Chemical reduction dependent dielectric properties and dielectric loss mechanism of reduced graphene oxide. *Carbon* 2018, **127**: 209–217.
- [51] Yu JJ, Liu SW, Duan GG, et al. Dense and thin coating of gel polymer electrolyte on sulfur cathode toward high performance Li-sulfur battery. *Compos Commun* 2020, **19**: 239–245.
- [52] Duan GG, Liu SW, Jiang SH, et al. High-performance polyamide-imide films and electrospun aligned nanofibers from an amide-containing diamine. *J Mater Sci* 2019, **54**: 6719–6727.
- [53] Cho WS, Cho MW, Lee JH, et al. Effects of h-BN additive on the microstructure and mechanical properties of AlN-based machinable ceramics. *Mater Sci Eng A* 2006, **418**: 61–67.
- [54] Chen C, Pan LM, Li XY, et al. Mechanical and thermal properties of graphene nanosheets/magnesia composites. *Ceram Int* 2017, **43**: 10377–10385.
- [55] Wang XL, He XB, Zhang R, et al. Interface and properties of copper matrix composites reinforced with TiC coated spherical graphite. *Mater Res Express* 2019, **6**: 116307.
- [56] Schlichting KW, Padture NP, Klemens PG. Thermal conductivity of dense and porous yttria-stabilized zirconia. *J Mater Sci* 2001, **36**: 3003–3010.
- [57] Ren LL, Zeng XL, Sun R, et al. Spray-assisted assembled spherical boron nitride as fillers for polymers with enhanced thermal conductivity. *Chem Eng J* 2019, **370**: 166–175.
- [58] Landon M, Thevenot F. Thermal conductivity of SiC-AlN materials. *J Eur Ceram Soc* 1991, 271–277.

- [59] Rutkowski P, Kata D, Jankowski K, et al. Thermal properties of hot-pressed aluminum nitride–graphene composites. *J Therm Anal Calorim* 2016, **124**: 93–100.
- [60] Baskut S, Cinar A, Turan S, Directional properties and microstructures of spark plasma sintered aluminum nitride containing graphene platelets. *J Eur Ceram Soc* 2017, **37**: 3759–3772.
- [61] Wang JJ, Yi XS. Effects of interfacial thermal barrier resistance and particle shape and size on the thermal conductivity of AlN/PI composites. *Compos Sci Technol* 2004, **64**: 1623–1628.
- [62] Guo X, Feng YR, Lin X, et al. The dielectric and microwave absorption properties of polymer-derived SiCN ceramics. *J Eur Ceram Soc* 2018, **38**: 1327–1333.
- [63] Zhou L, Cui S, Zhai Y, et al. Dielectric and microwave absorption properties of plasma sprayed Cr/Al<sub>2</sub>O<sub>3</sub> composite coatings. *Ceram Int* 2015, **41**: 14908–14914.
- [64] Li W, Li XC, Gong W, et al. Construction of multiple heterogeneous interface and its effect on microwave absorption of SiBCN ceramics. *Ceram Int* 2020, **46**: 7823–7832.
- [65] Qin M, Lan D, Wu GL, et al. Sodium citrate assisted hydrothermal synthesis of nickel cobaltate absorbers with tunable morphology and complex dielectric parameters toward efficient electromagnetic wave absorption. *Appl Surf Sci* 2020, **504**: 144480.
- [66] Long L, Xu JX, Luo H, et al. Dielectric response and electromagnetic wave absorption of novel macroporous short carbon fibers/mullite composites. *J Am Ceram Soc* 2020, **103**: 6869–6880.
- [67] Calame JP, Abe DK, Levush B, et al. Broadband complex dielectric permittivity of porous aluminum silicate–pyrolytic carbon composites. *J Am Ceram Soc* 2005, **88**: 2133–2142.
- [68] Li XL, Yin XW, Song CQ, et al. Self-assembly core–shell graphene-bridged hollow MXenes spheres 3D foam with ultrahigh specific EM absorption performance. *Adv Funct Mater* 2018, **28**: 1803938.
- [69] Yu ZJ, Lv X, Mao KW, Yang YJ, et al. Role of in-situ formed free carbon on electromagnetic absorption properties of polymer-derived SiC ceramics. *J. Adv.*

*Ceram.* 2020, **9**: 617–628.

[70] Liu JL, Liang HS, Wu HJ. Hierarchical flower-like Fe<sub>3</sub>O<sub>4</sub>/MoS<sub>2</sub> composites for selective broadband electromagnetic wave absorption performance. *Composites, Part A* 2020, **130**: 105760.

[71] Zhou W, Yin RM, Long L, et al. Enhanced high-temperature dielectric properties and microwave absorption of SiC nanofibers modified Si<sub>3</sub>N<sub>4</sub> ceramics within the gigahertz range. *Ceram Int* 2018, **44**: 12301–12307.

[72] Lou ZC, Li R, Wang P, et al. Phenolic foam-derived magnetic carbon foams (MCFs) with tunable electromagnetic wave absorption behavior. *Chem Eng J* 2020, **391**: 123571.

## Figures

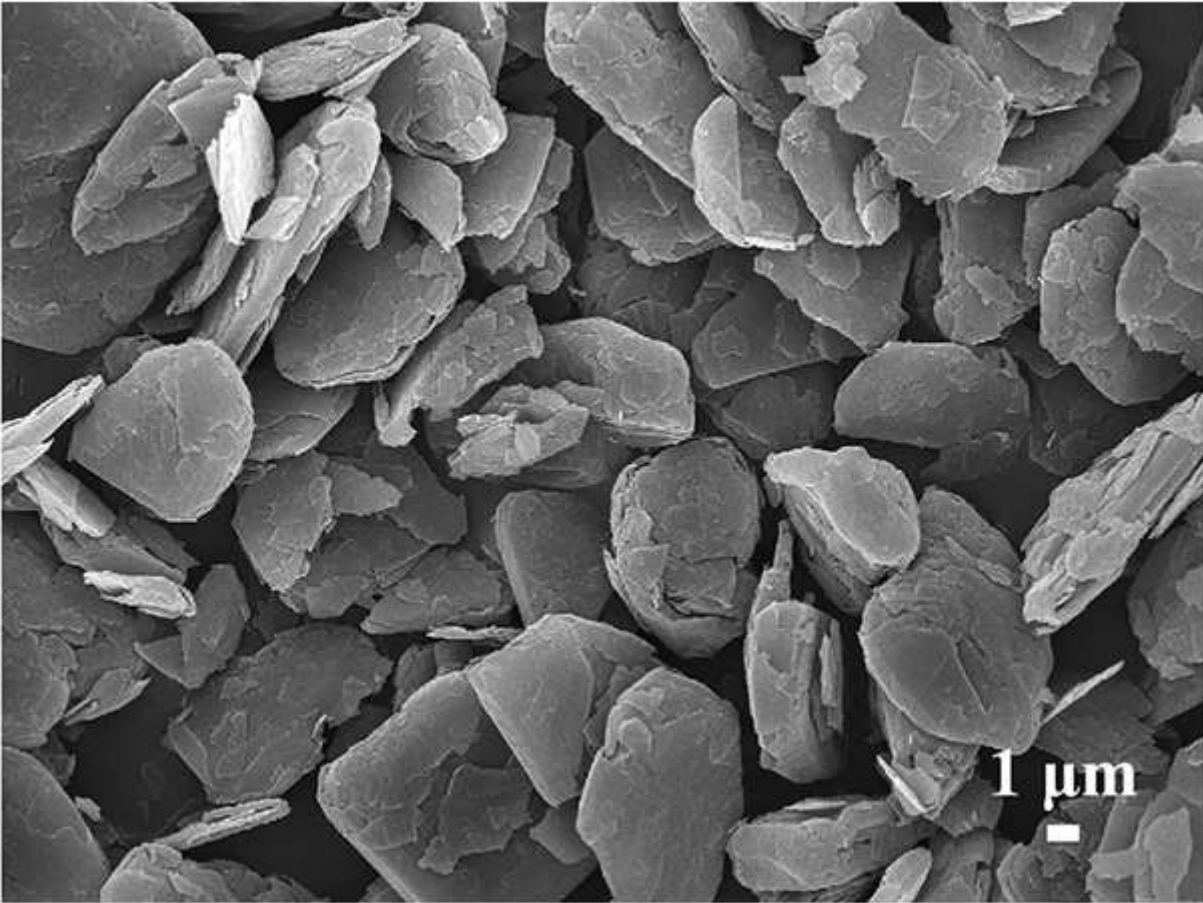


Figure 1

Micro-morphology of spherical graphite raw material

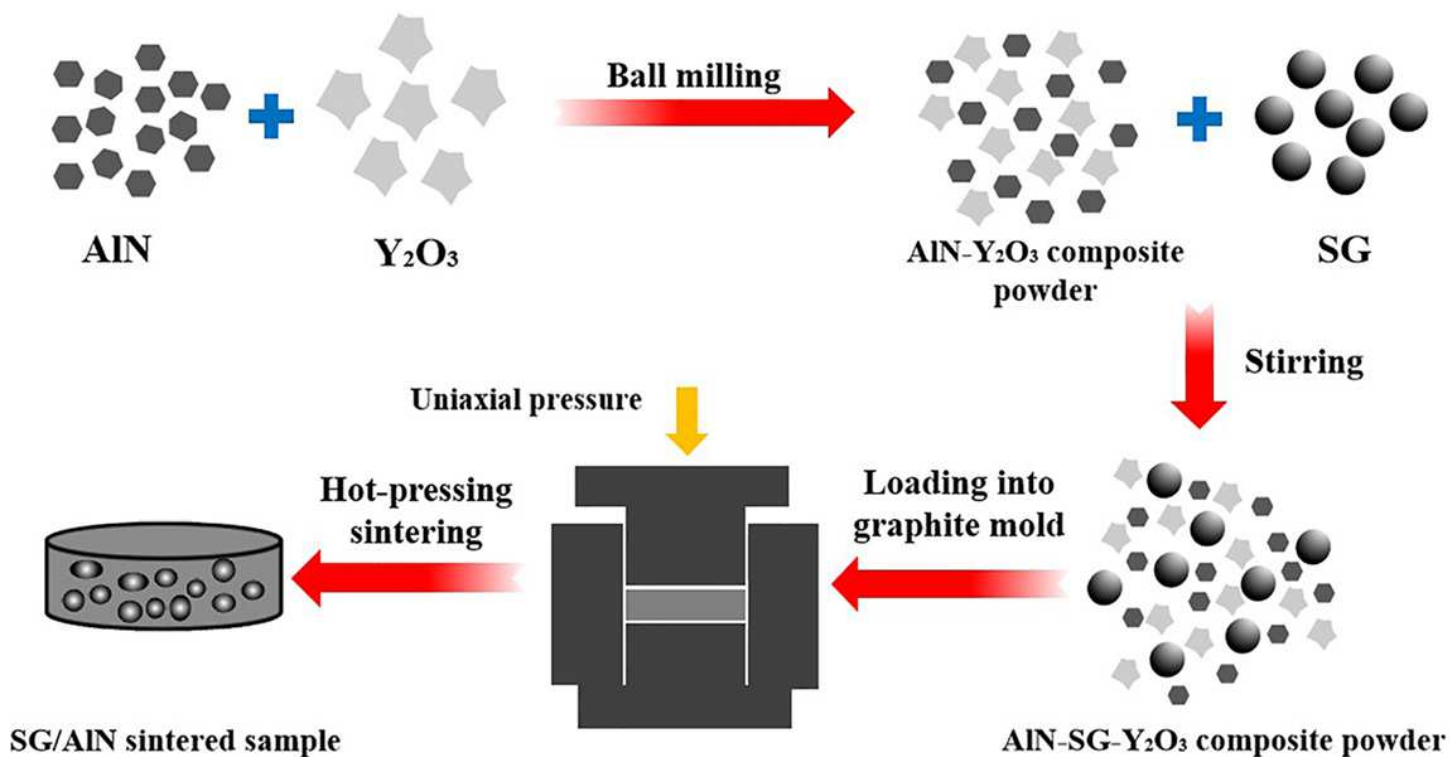


Figure 2

Schematic of the preparation process for fabricating the SG/AlN composites

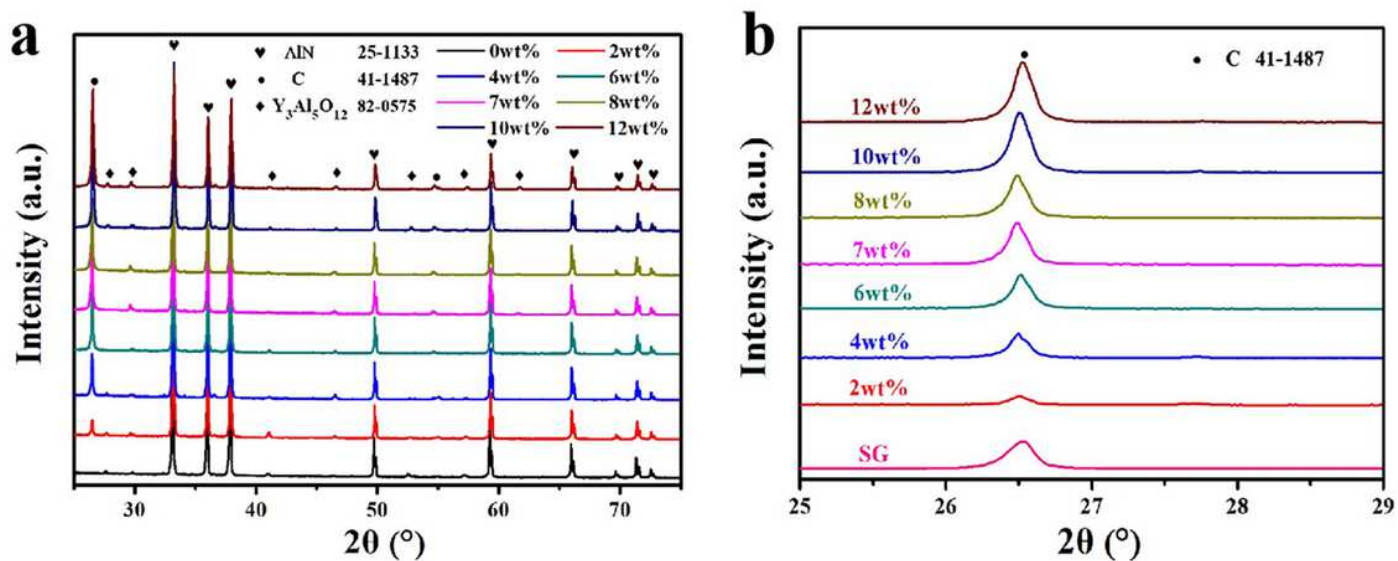
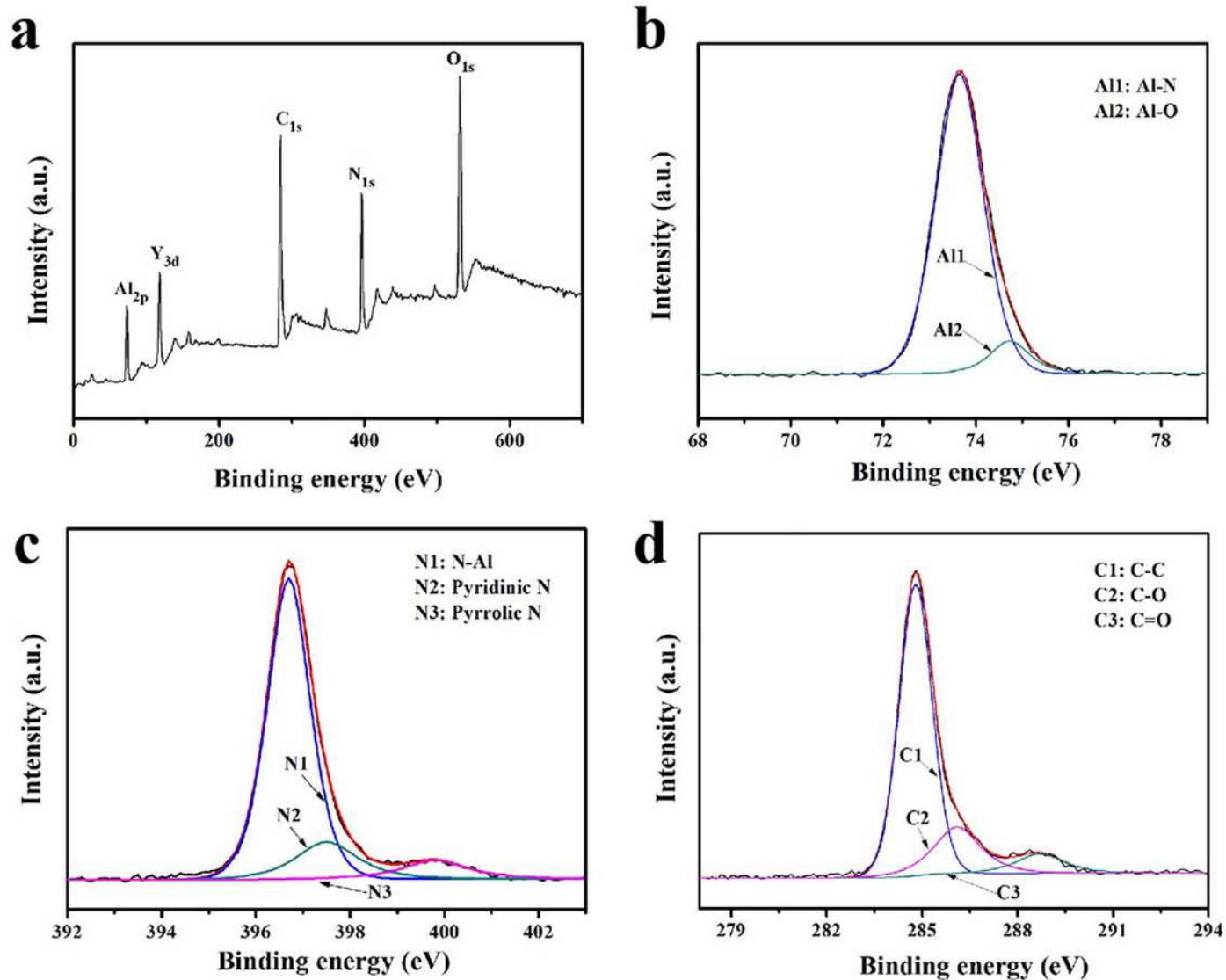


Figure 3

(a) XRD patterns of SG/AlN composites with different SG contents, (b) XRD patterns of SG raw powder and SG/AlN composites with different SG contents at 25 to 29 degrees



**Figure 4**

(a) XPS survey spectra of 4 wt% composite, (b–d) are the spectra of Al 2p, N 1s and C 1s, respectively

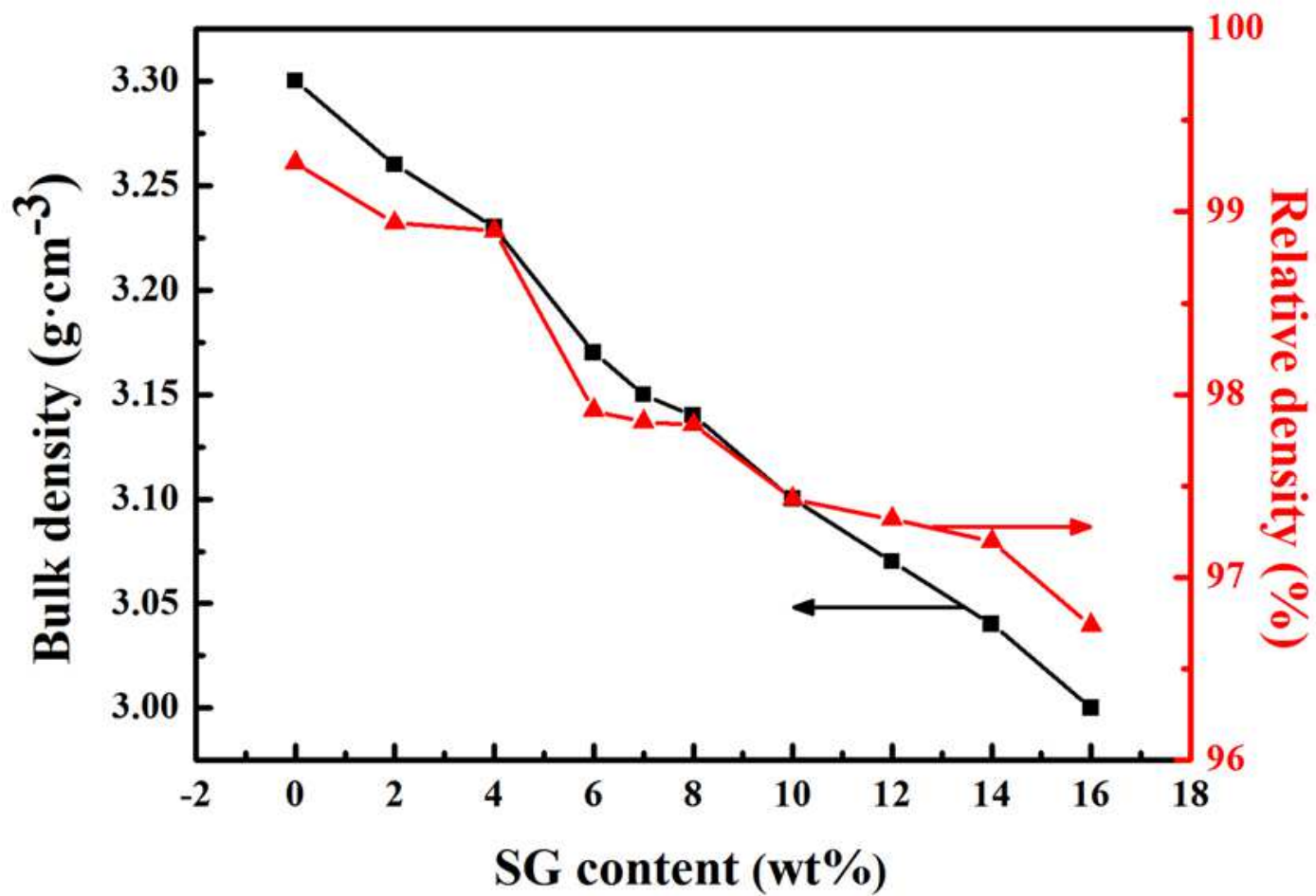


Figure 5

Bulk density and relative density of SG/AlN composites with different SG contents

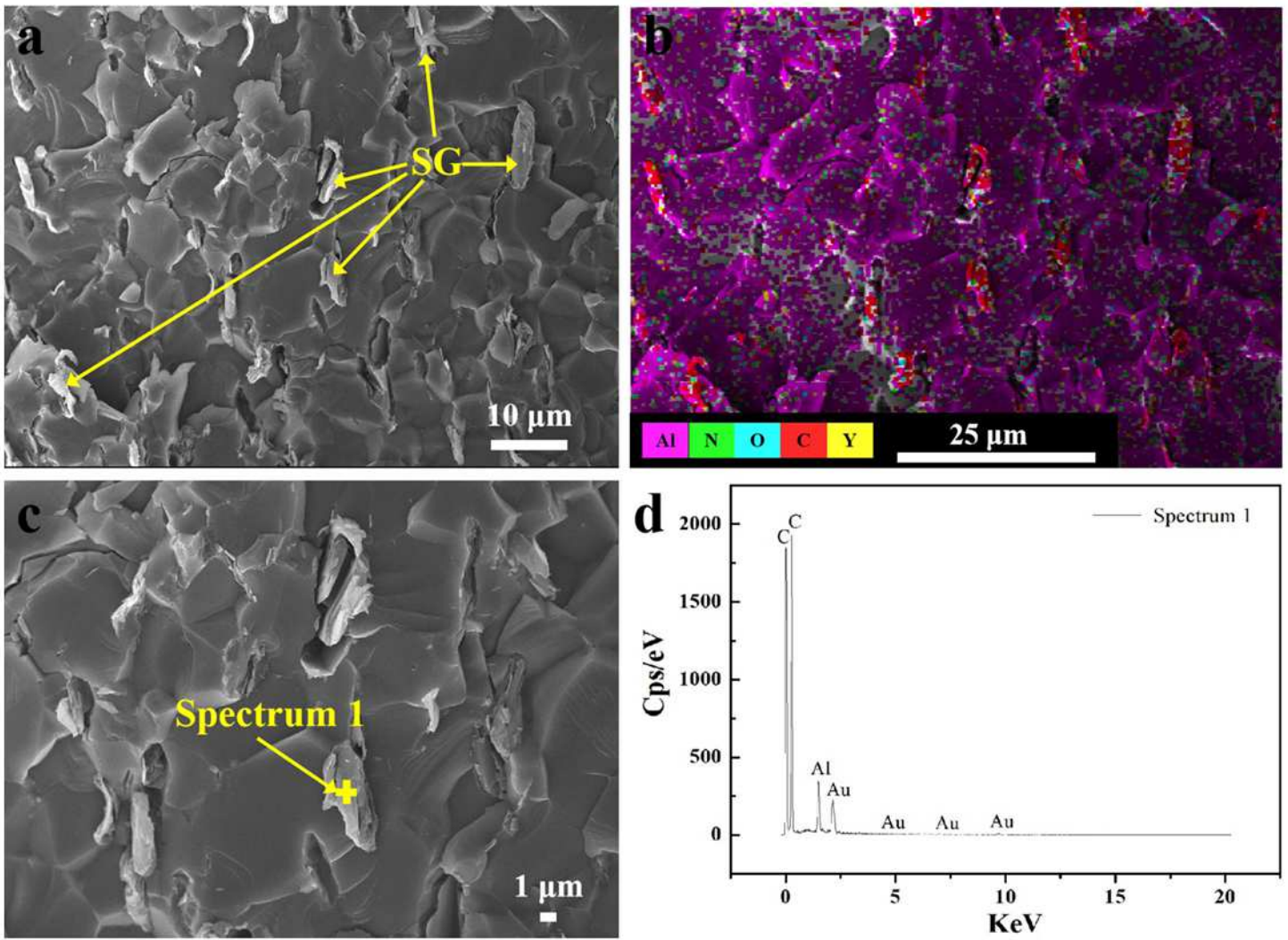


Figure 6

(a) Microstructure, (b) EDS mapping, (c) high-resolution microstructure and (d) EDS diagrams of 4 wt% SG/AlN composite without ultrasonic cleaning

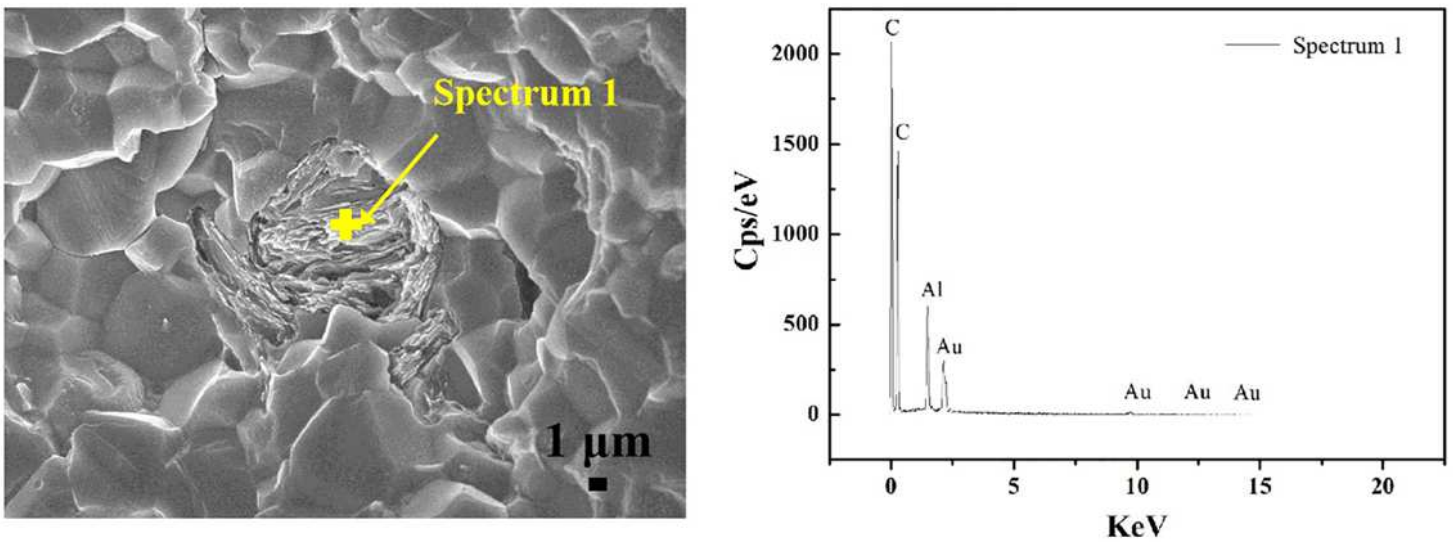


Figure 7

Microstructure (ultrasonic cleaning) and EDS diagrams of 4 wt% SG/AlN composite

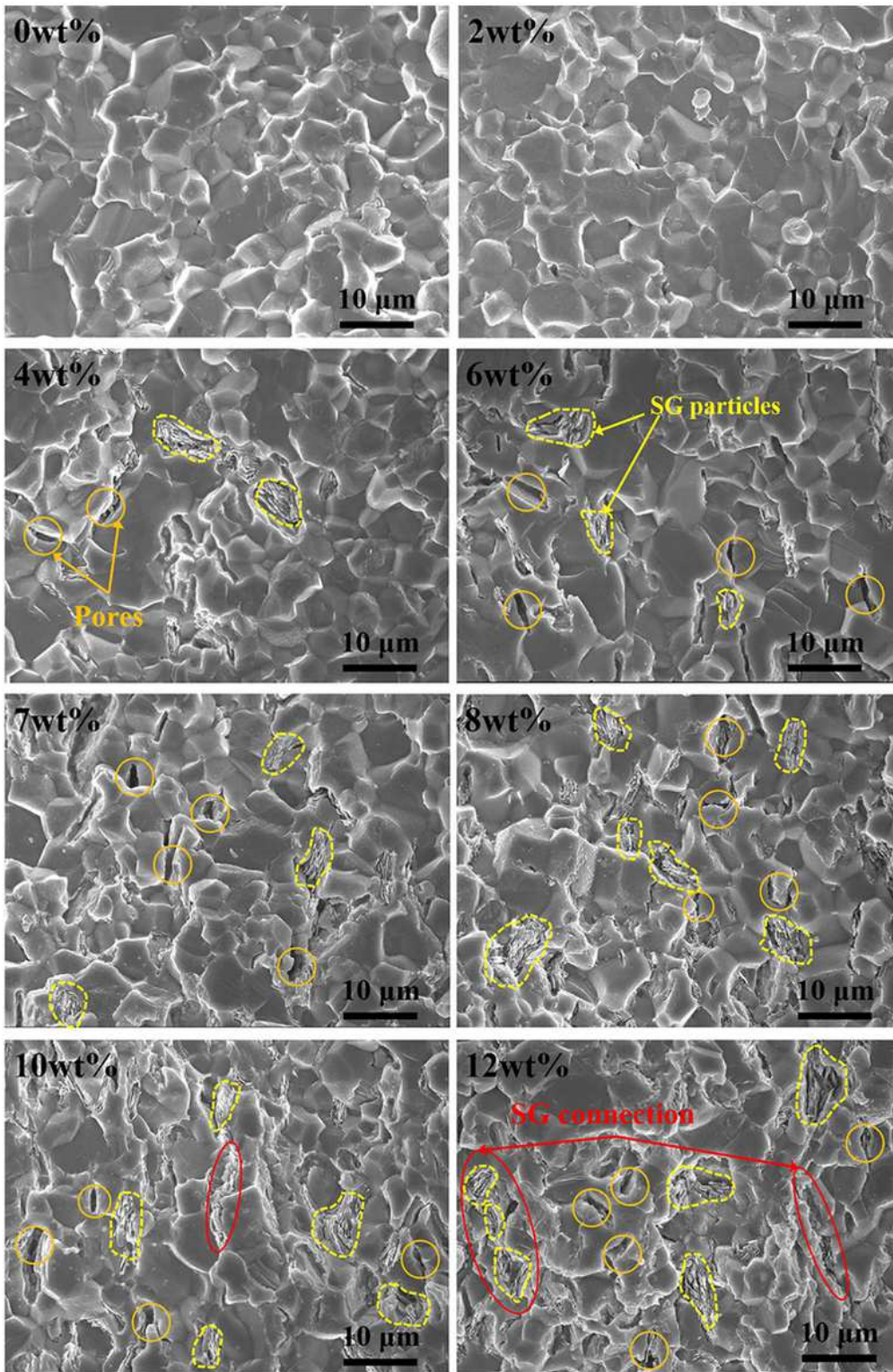


Figure 8

Fracture morphology of SG/AlN composites with different SG contents

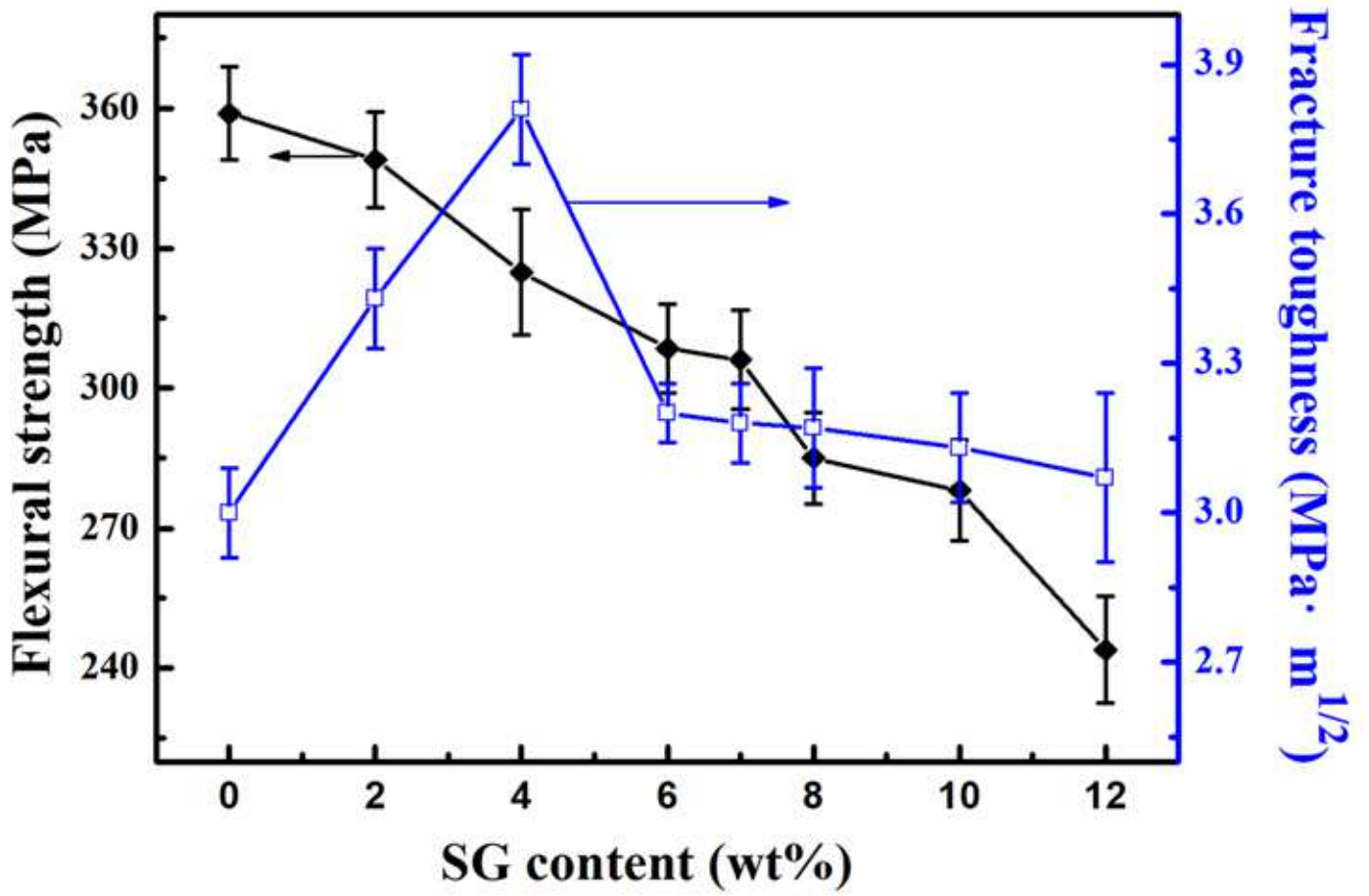


Figure 9

Mechanical properties of SG/AlN composites with different SG contents

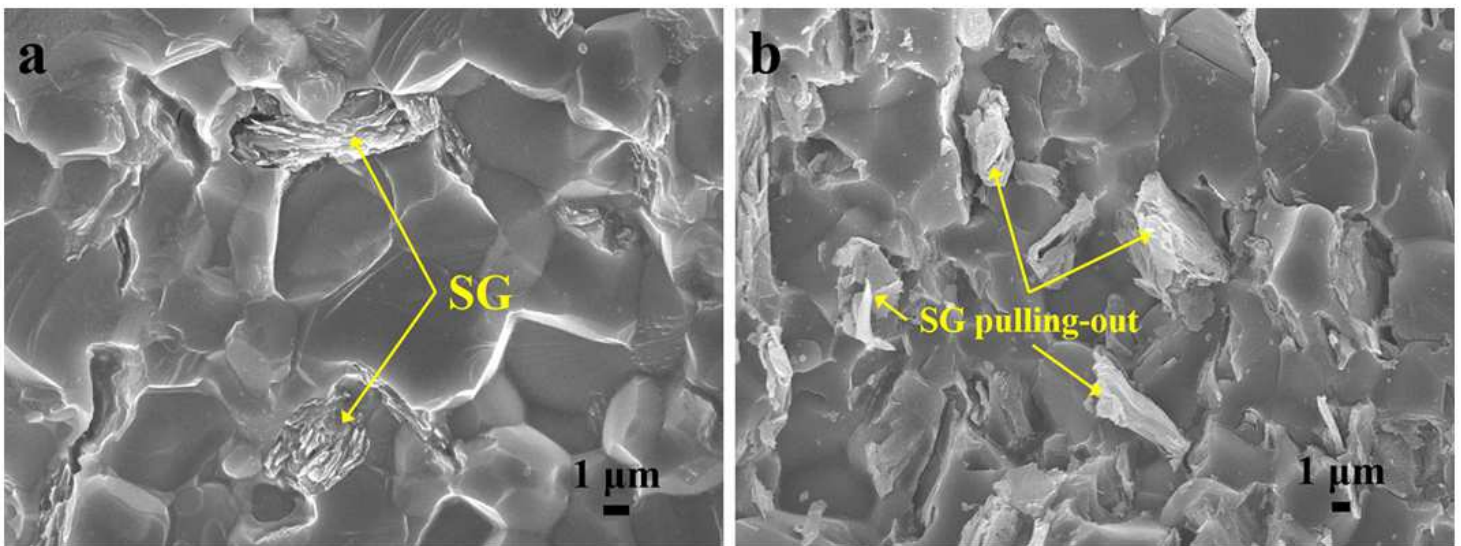


Figure 10

High-resolution fracture morphology of 4 wt% SG/AlN composite, (a) ultrasonic cleaning, (b) without ultrasonic cleaning

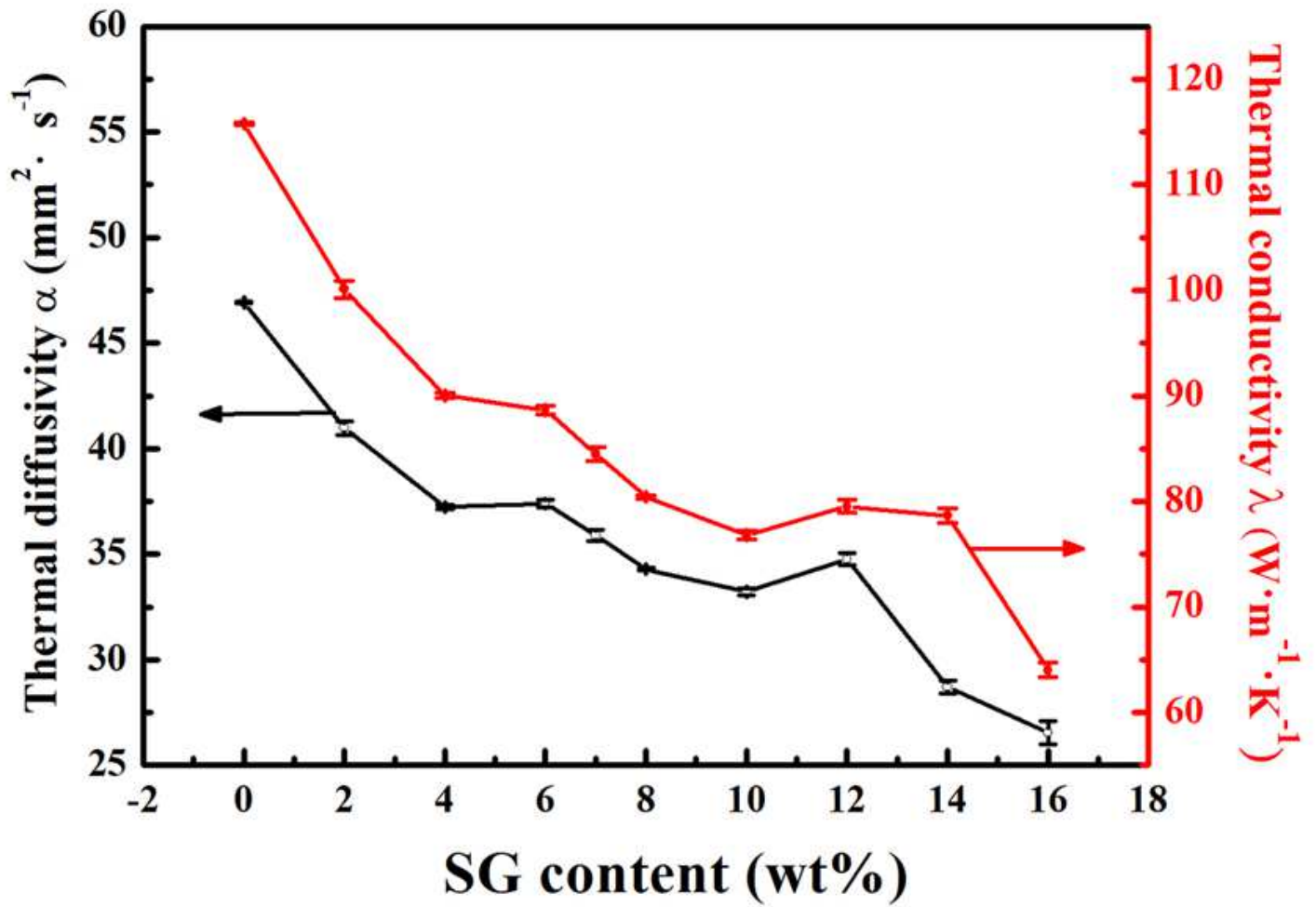


Figure 11

Thermal diffusivity and thermal conductivity of SG/AlN composites with different SG contents

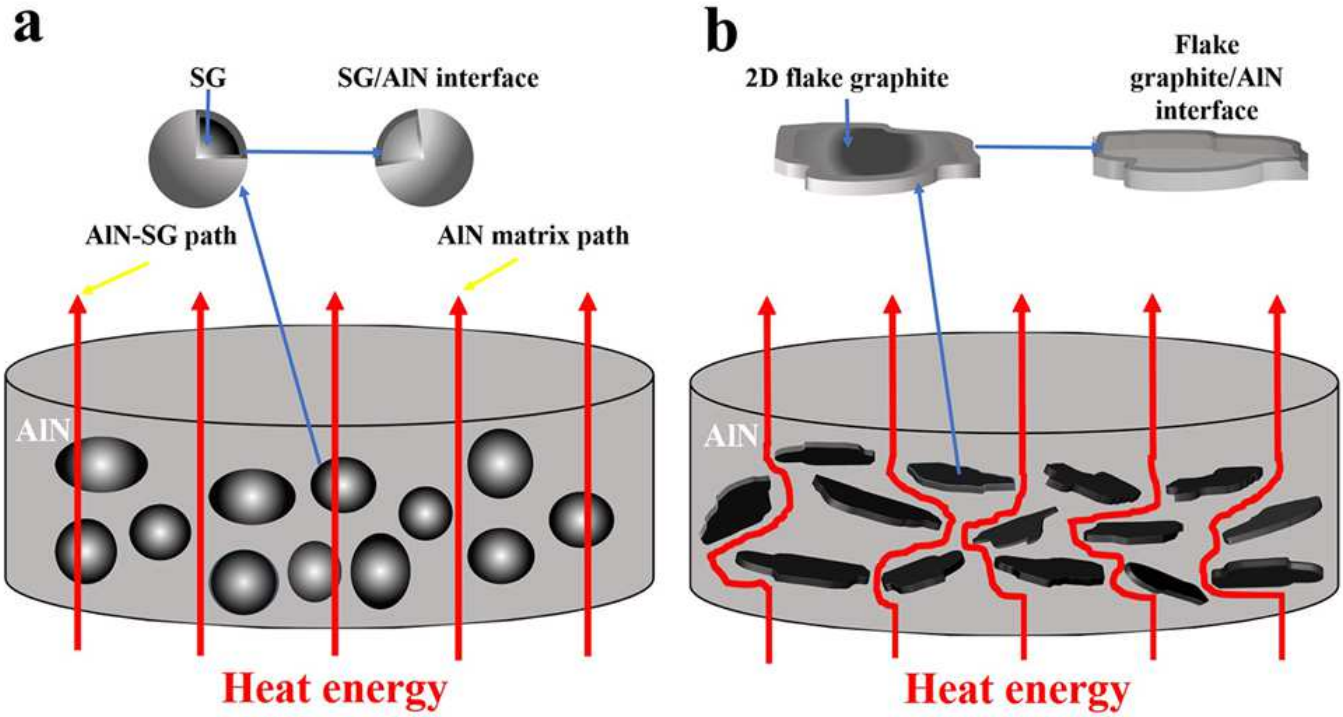


Figure 12

The schematic diagram of thermally conductive path in composite filled with different shaped second phase, (a) spherical graphite, (b) 2D flake graphite

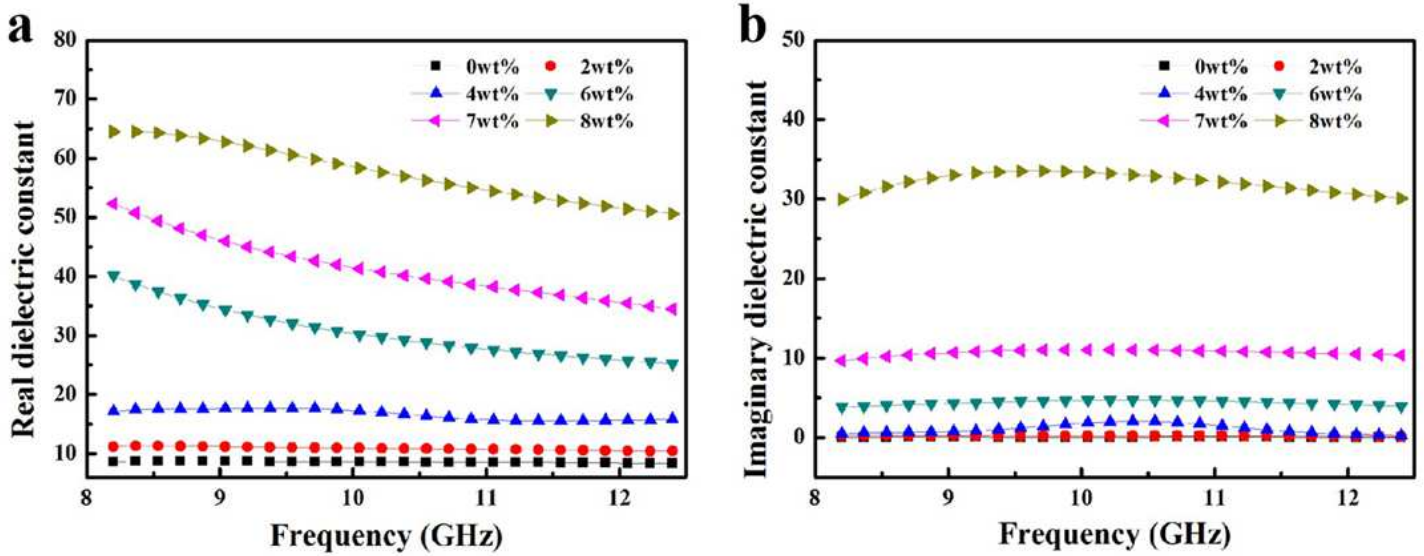


Figure 13

Dielectric constant of SG/AlN composites with different SG contents

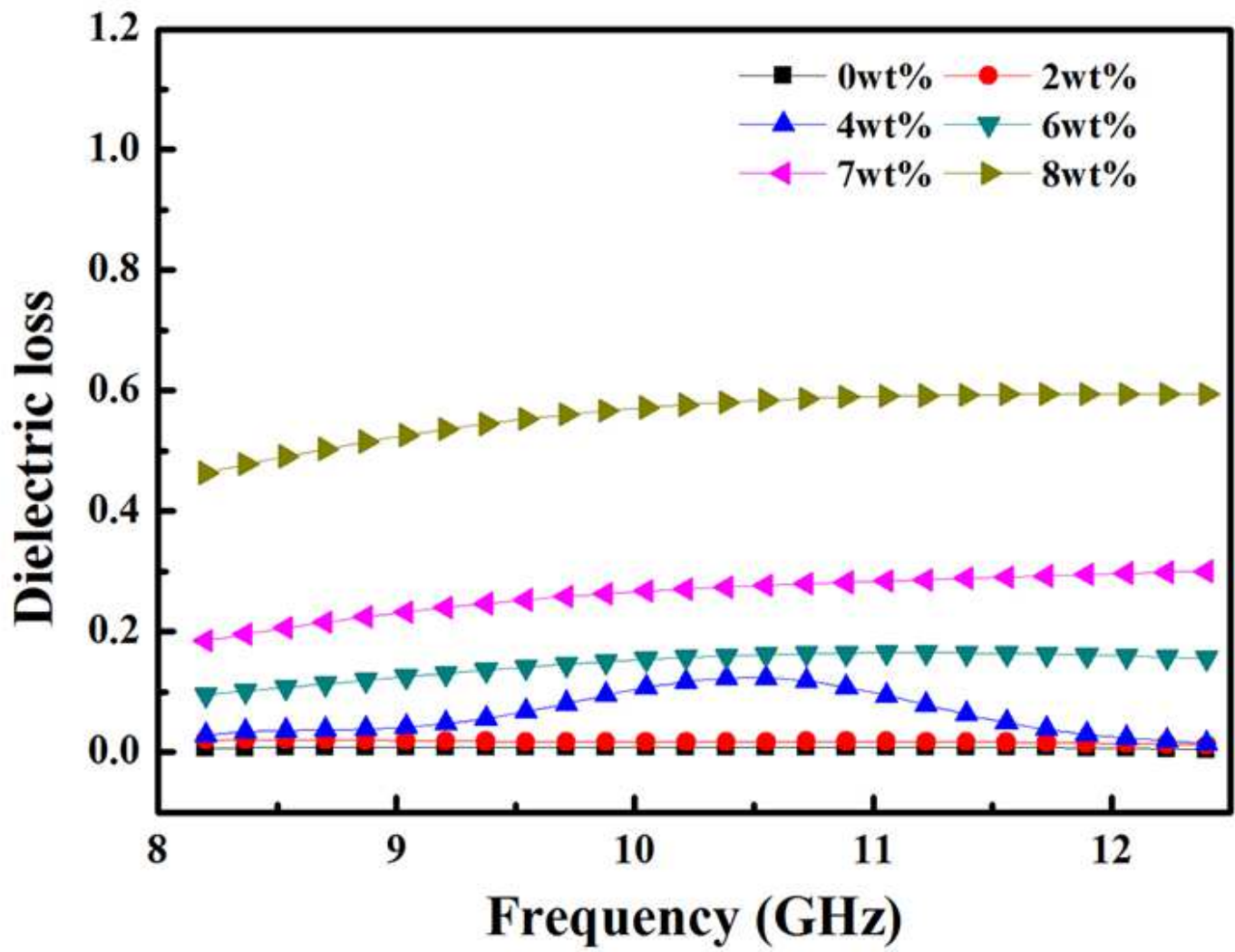
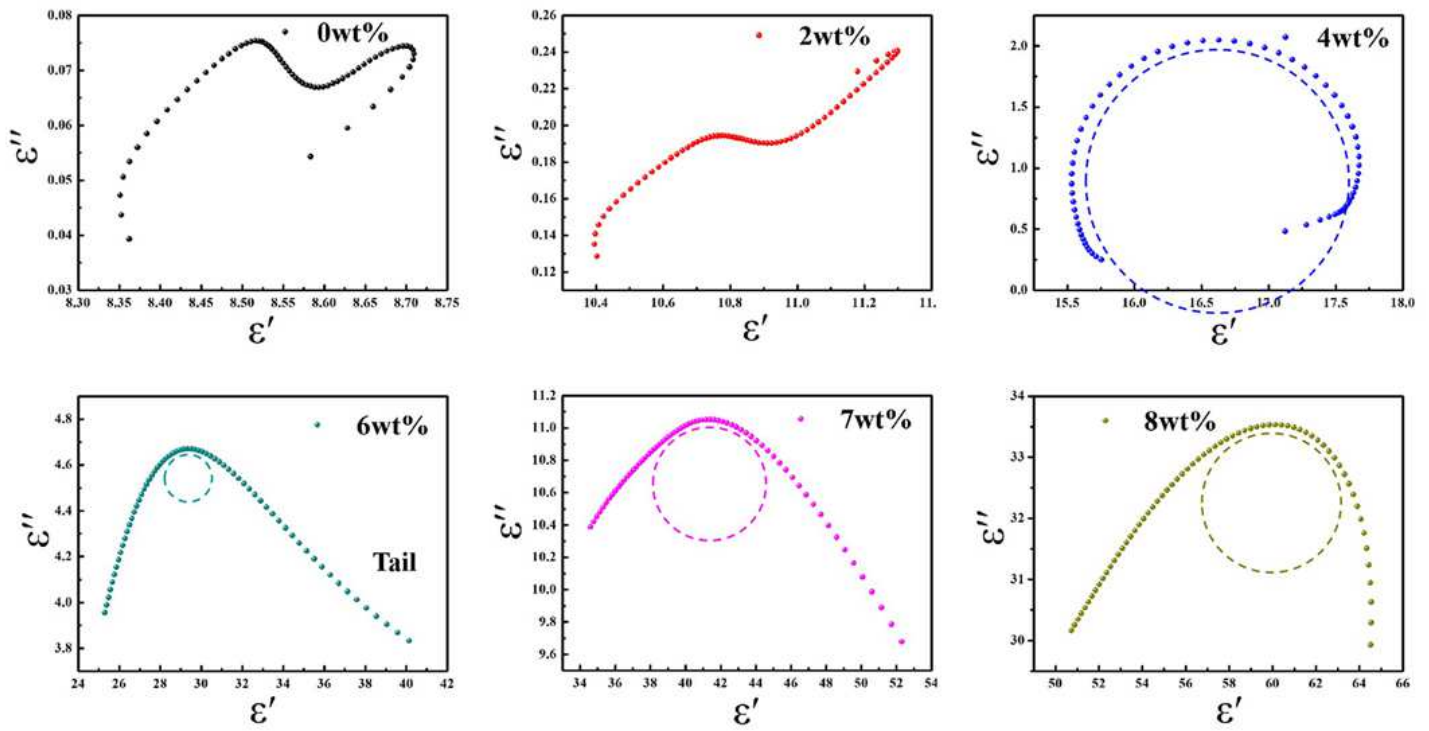


Figure 14

Dielectric loss of SG/AlN composites with different SG contents



**Figure 15**

The  $\epsilon'$ - $\epsilon''$  curves of SG/AlN composites with different SG contents

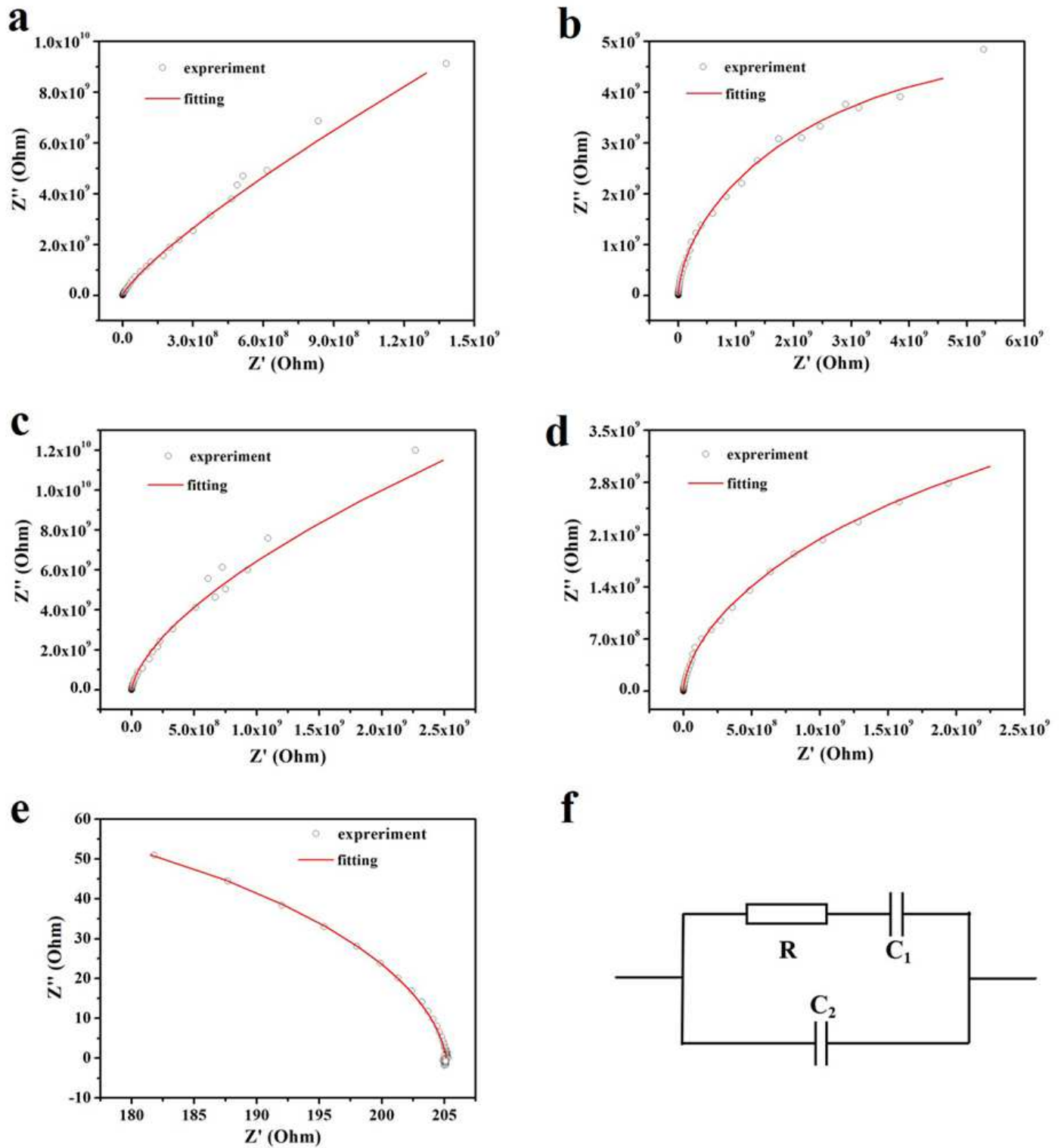


**Figure 16**

The impedance spectrum of the SG/AlN composites (a) 2 wt%, (b) 4 wt%, (c) 6 wt%, (d) 7 wt%, (e) 8 wt%, and (f) equivalent circuit model of a micro-region in the composites

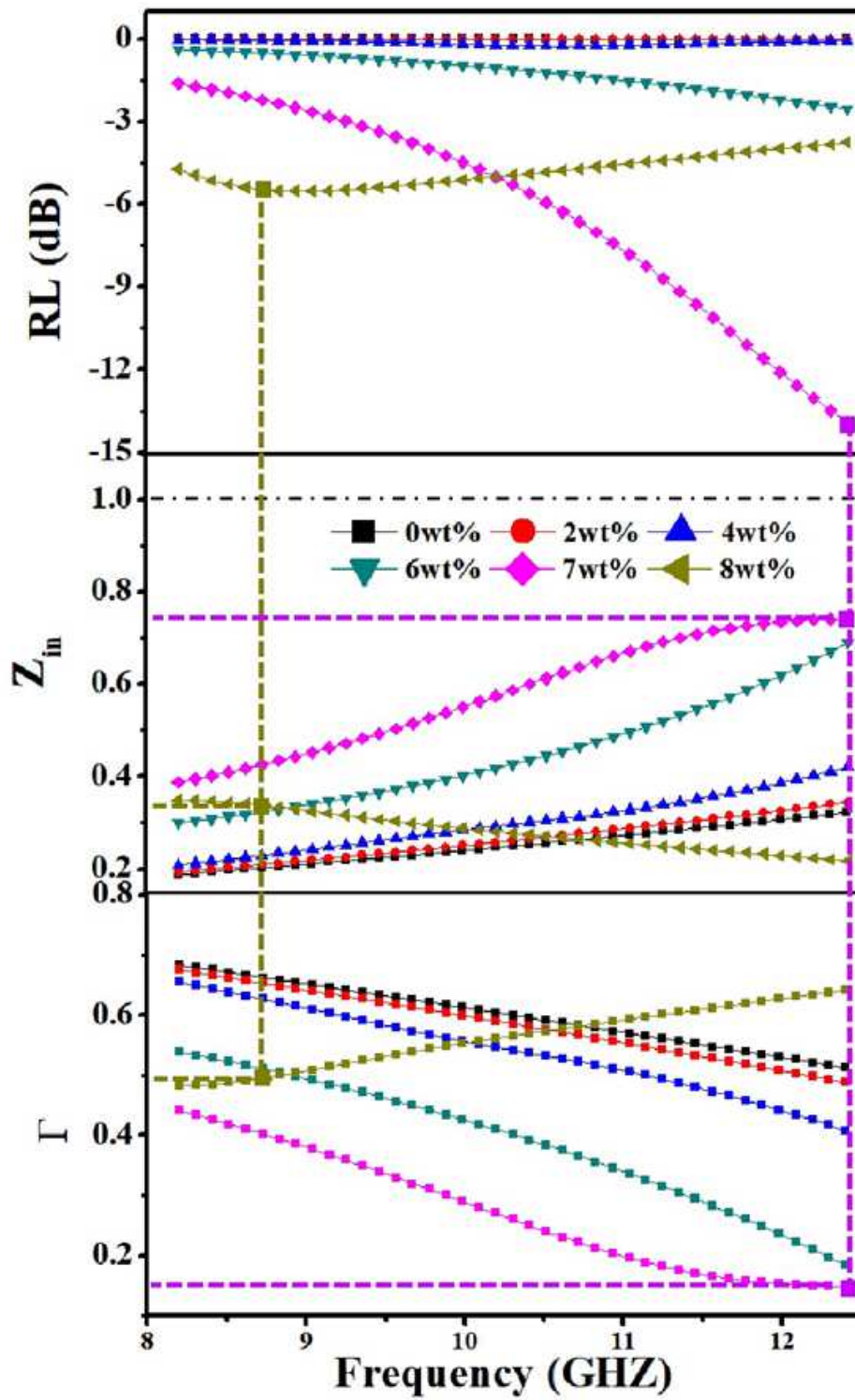


Figure 17

Reflection loss, incident impedance and reflection coefficient of SG/AlN composites with different SG contents